Article:
Del Vecchio, J., Lang, K., Robins, C. et al. (2018) Storage and weathering of landslide debris in the eastern San Gabriel Mountains, California, USA: implications for mountain solute flux. Earth Surface Processes and Landforms, 43 (13). pp. 2724-2737. ISSN: 0197-9337

https://doi.org/10.1002/esp.4427

Storage and weathering of landslide debris in the eastern San Gabriel Mountains, California, USA: implications for mountain solute flux

Joanmarie Del Vecchio*, Karl A. Lang, Colin R. Robins, Chris McGuire, Edward Rhodes

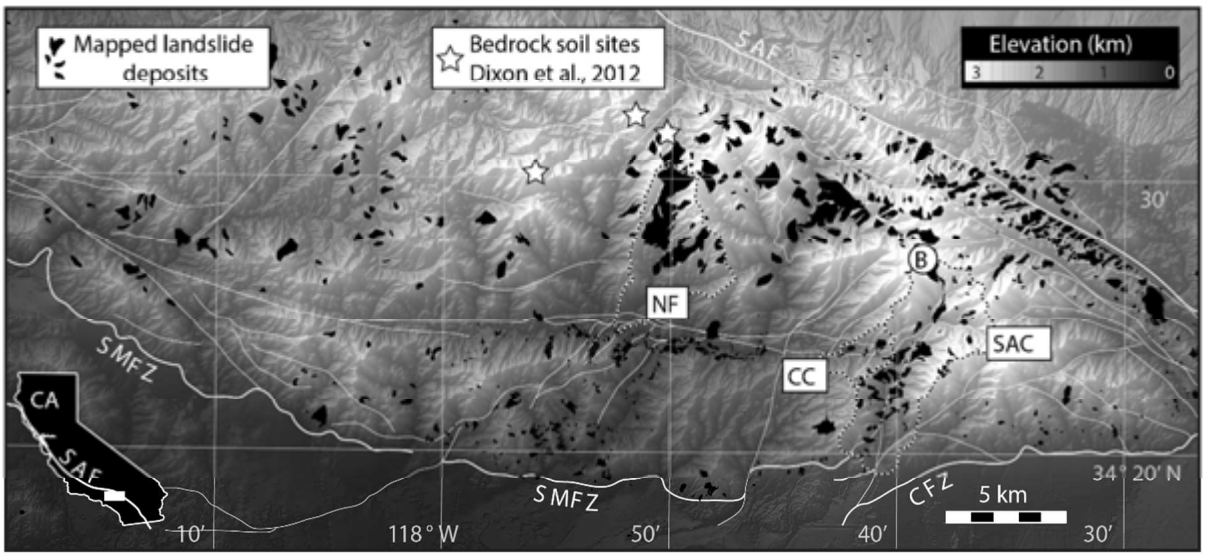

Here we present new observations of landslide debris storage in a steep, rapidly eroding landscape. We map landslide debris forming planar, low-sloping deposits with soil development. Luminescence burial dating indicates debris may persist over 10^4 yr timescales. Geochemical and textural analyses of debris surface soils indicates enhanced weathering. We argue that landslide debris porosity may be an important control on long-term solute flux

Storage and weathering of landslide debris in the eastern San Gabriel Mountains, California, USA: implications for mountain solute flux

Joanmarie Del Vecchio[1†*], Karl A. Lang[1‡], Colin R. Robins[2], Chris McGuire[3], Edward Rhodes[4]
1. Geology Department, Pomona College, 185 E 6th St., Claremont, CA, 91711, USA
2. W. M. Keck Science Department, Claremont McKenna, Pitzer, and Scripps Colleges, 925 N. Mills Ave, Claremont, CA, 91711, USA
3. Department of Earth, Planetary, and Space Sciences, University of California Los Angeles, 595 Charles Young Drive East, Los Angeles, CA 90095, USA
4. Department of Geography, University of Sheffield, Winter Street, Sheffield, S10 2TN, UK
†Now at Department of Geosciences, Pennsylvania State University, University Park, Pennsylvania 16802, USA.
‡Now at Department of Geosciences, University of Tübingen, Wilhelmstraße 56, Tübingen, 72076, Germany.
* Corresponding author at: Department of Geosciences, Pennsylvania State University, University Park, Pennsylvania 16802, USA. Email: joanmarie@psu.edu

Abstract

The weathering of silicate minerals in mountain landscapes provides a critical source of chemical solutes in the global biogeochemical cycles that sustain life on Earth. Observations from across Earth's surface indicate that the greatest flux of chemical solute is derived from rapidly eroding landscapes, where landsliding often limits the development of a continuous soil cover. In this study, we evaluate how weathering of landslide debris deposits may supplement the chemical solute flux from rapidly eroding, bedrock-dominated landscapes. We present new measurements of depositional surface and soil morphology, soil geochemistry, and luminescence-based depositional ages from debris stored in Cow Canyon, a tributary to the East Fork of the San Gabriel River in the eastern San Gabriel Mountains of California. Cow Canyon deposits include locally derived debris emplaced by dry colluvial and debris flow processes. Deposits have planar, low-angle, sloping surfaces with soils exhibiting a greater degree of weathering than nearby soils formed on bedrock. A ~30-40 ka

depositional age of Cow Canyon deposits exceeds the estimated recurrence time for the largest landslides in the San Gabriel Mountains, suggesting the stored landslide debris may be a persistent source of chemical solute in this landscape. To quantitatively explore the significance of landslide debris on the landscape solute flux, we predict the flux of chemical solute from bedrock and debris soils using a generic, time-dependent model of soil mineral weathering. Our modeling illustrates that debris soils may be a primary source of chemical solute for a narrow range of conditions delimited by the initial landslide debris porosity and the comparative soil age. Broadly, we conclude that while landslide debris may be an important local reservoir of chemical solute, it is unlikely to dominate the long-term solute flux from rapidly eroding, bedrock-dominated landscapes.

Keywords: landscape evolution, landslides, luminescence dating, San Gabriel Mountains, soil

1. Introduction

The denudation of Earth's surface is a critical source of chemical solute in global biogeochemical cycles. Weathering of silicate minerals releases constituent ions into solution (Bluth and Kump, 1994; Godsey et al., 2009) providing nutrients to support autotrophic life and sequester carbon dioxide (Urey, 1952; Walker et al., 1981; Berner et al., 1991), regulating global climate over geologically significant timescales (Chamberlin, 1899; Raymo and Ruddiman, 1992; Kump et al., 2000). As researchers work to disentangle the interrelationships between tectonic, climatic, and surface processes, the

significance of weathering in mountain landscapes remains debated (Willenbring et al., 2013; Maher and Chamberlain, 2014; Warrick et al., 2014). In particular, analytical models developed to predict solute fluxes from stable, soil-covered landscapes (Ferrier and Kirchner, 2008; Gabet and Mudd, 2009) fail to explain elevated solute fluxes in rapidly eroding landscapes where landsliding restricts the development of a continuous soil cover (West, 2012; Larsen et al., 2014a). This study contributes to this debate on the specific role of weathering in mountain landscapes with analysis of the contribution of chemical solute from soils developed on stored landslide debris. We provide new observations from soils developed on partially reworked landslide debris deposits in the eastern San Gabriel Mountains and evaluate the contribution such deposits may have on the long-term (>10^5 yr) flux of chemical solute from rapidly eroding, bedrock-dominated landscapes.

1.1 Weathering in mountain landscapes

Analytical models of mineral weathering in a steady-state soil profile predict a nonlinear relationship between the rate of surface erosion and the flux of chemical solute from a mountain landscape (Figure 1). In slowly eroding landscapes characterized by low hillslope angles, this relationship is positive and approximately linear (Riebe et al., 2001; Riebe et al., 2004) but becomes increasingly nonlinear as progressive soil development restricts the supply of fresh mineral surface area available for weathering (Millot et al., 2002; White and Brantley, 2003; West et al., 2005). The relationship between erosion rate and chemical solute flux turns abruptly negative in steep, rapidly eroding landscapes (Gabet and Mudd, 2009) where hillslope material

transport transitions from diffusive (i.e. soil creep dominated) to advective processes (i.e. landsliding, Montgomery and Brandon, 2002; Roering et al., 2007), restricting the development of a continuous soil cover. In landscapes where the frequency of landsliding effectively prohibits the development of a continuous soil cover, hillslopes are dominated by exposed bedrock (DiBiase et al., 2012; Heimsath et al., 2012a) and the contribution of chemical solute from thin or patchy bedrock soils should approach zero.

In contrast to model predictions, measurements of chemical solute flux compiled from landscapes across Earth's surface remain high in rapidly eroding landscapes (West, 2012; Larsen et al., 2014a). Observations from steep, bedrock-dominated portions of the eastern San Gabriel Mountains suggest that this discrepancy may be explained by enhanced weathering in saprolitized bedrock (Dixon et al., 2012) or locally elevated pedogenic rates where thin, patchy soils remain (Heimsath et al., 2012b). Geologic mapping of the San Gabriel Mountains shows that landslide deposits (Dibblee and Minch, 2002; Morton and Miller, 2003) and reworked landslide debris (Scherler et al., 2016) are a significant component of steep, high relief portions of the landscape (Figure 2). Here we consider that soils developed on stored and partially reworked landslide debris may provide an alternative and previously unexplored source of chemical solute that partially explains global observations of high solute fluxes from rapidly eroding landscapes.

1.2 The San Gabriel Mountains

The San Gabriel Mountains are a tectonically active, semi-arid to sub-humid mountain range located at the northern margin of the Los Angeles basin in southern California (Bull, 1991). The mountains primarily comprise crystalline plutonic and metamorphic basement units (Morton and Miller, 2003; Yerkes et al., 2005) uplifted since approximately 6 Ma (Nourse, 2002) by active range-bounding thrust faults (e.g. the Sierra Madre and Cucamonga fault systems, Crowell, 1982; McFadden, 1982; Dolan et al., 1996; Morton and Miller, 2003) in a restraining bend of the San Andreas Fault system. Erosion rates determined by thermochronology (Blythe, 2002) and cosmogenic radionuclides (DiBiase et al., 2010) increase with topographic relief, river channel steepness, and mean hillslope angles eastward across the mountains (Spotila and House, 2002). Detailed mapping of bedrock exposure in the San Gabriel Mountains (DiBiase et al., 2012) demonstrates a positive relationship between catchment hillslope angle and percentage bedrock exposure. In the eastern San Gabriel Mountains near Mt. San Antonio, hillslope angles frequently exceed ~30° and erosion rates as high as ~1000 m/Ma are primarily achieved by landsliding (Lavé and Burbank, 2004) on bedrock-dominated hillslopes (Heimsath et al. 2012). Unlike humid landslide-dominated landscapes (e.g. Moon et al., 2011; Larsen and Montgomery, 2012), the San Gabriel Mountains exhibit high exhumation rates in a relatively dry climate, providing the opportunity to study how hillslope processes specifically contribute to global denudational fluxes.

Thick deposits of primary and reworked landslide debris are common in the eastern San Gabriel Mountains (Dibblee and Minch, 2002; Morton and Miller, 2003) where they are interpreted to originate from large magnitude landslide events (Morton et

al., 1989; Morton and Miller, 2003; Scherler et al., 2016). In landscapes where landsliding is the dominant erosion process, the long-term debris flux is defined by the landslide frequency-magnitude relationship (Hovius et al., 1997; Niemi et al., 2005) . If river channels are adjusted to a long-term average debris flux, then episodic large magnitude events may overwhelm the capacity of rivers to transport landslide debris (Ouimet et al., 2008) storing partially reworked landslide debris in low-sloping deposits above river channels (Yanites et al., 2010). Landslide deposits mapped in eastern San Gabriel Mountain catchments form similarly lower sloping deposits (Figure 3) that may provide relatively stable surfaces for locally enhanced pedogenesis, supplementing the chemical solute flux from an otherwise unstable, bedrock-dominated landscape.

1.3 Landslide debris in Cow Canyon

Our analysis focuses on landslide debris deposited in Cow Canyon, a ~10 km^2 tributary to the East Fork of the San Gabriel River. Three poorly consolidated deposits collectively interpreted as Quaternary elevated older alluvial gravel (Dibblee and Minch, 2002) or late Holocene to middle Pleistocene landslide deposits (Morton and Miller, 2003) occur at similar elevation on the north side of the canyon. Vegetation on the deposit surface is typical chaparral, including dense stands of shrubs including scrub oak, California sagebrush, chamise, chapparal yucca, manzanita and others (US National Park Service, 2013). The sparser vegetation on surrounding steeper hillslopes is limited to trees (e.g. sugar pine *P. lambertiana* and others) in steep debris chutes and on north-facing slopes. The surfaces of these deposits are densely vegetated, remarkably planar and dip at similar orientations downstream, suggesting they may be

relicts from a more extensive valley fill surface. Prior aggradation of Cow Canyon may be related to damming and reorganization of San Antonio Canyon (e.g. Ehlig, 1958; Morton et al., 1989; Morton and Miller, 2003), although this relationship remains speculative. Though landslide scars and recent debris are common in the eastern San Gabriel Mountains, the preservation of older, weathered deposits is rare. Thus, we target these otherwise-transient features for further study.

Soils in Cow Canyon exhibit distinctly reddened yet morphologically simple, sandy to gravelly profiles. Soils are mapped by the Natural Resource Conservation Service as Soil Survey Unit 316, including exposed bedrock, Haploxerolls and Chilao family soils (Soil Survey Staff, 2014). Unit 316 represents up to ~40% exposed bedrock with remaining surfaces exhibiting one or more gravelly, well-drained Xerorthents (~41%), Haploxerolls (~15%), and/or Haploxerepts (2%), none of which exhibit strongly illuviated B horizons. Chilao family soils specifically are described as having a ~13 cm gravelly-loam A horizon atop a ~30 cm C horizon of gravelly sand. Soil mineralogy is representative of the crystalline basement source rocks and primarily includes quartz, hornblende, micas, and minor magnetite (McFadden, 1982). Detailed field photographs of the deposits, soils and vegetation are available as Supplemental Figures.

To interpret the origin, age and susceptibility of deposits to soil development, we expand upon this previous work with detailed Structure from Motion modeling of a debris surface, and new measurements of soil morphology, geochemistry, clay mineralogy and luminescence-based depositional ages.

2. Methods

We constructed structure-from-motion photogrammetry models (Westoby et al., 2012) to visualize and quantitatively describe the surface morphology of the largest Cow Canyon deposit and identify areas of surface degradation. We qualitatively described deposit thickness and sedimentology along the deposit, as well as four soil profiles from intact portions of the deposit surface that capture the full variability in the surface catena. Description of soil profile and horizon morphology were made in the field from cleaned, vertical road cut exposures between 1040 to 1187 m elevation following the protocols of Schoeneberger et al. (2012). To quantitatively measure physical and chemical soil properties including elemental changes in response to chemical weathering, bulk soil samples were collected from each soil horizon for laboratory analysis of soil texture, color, clay mineralogy, major and trace element concentrations. Bulk soil samples were sieved to < 2 mm and air-dried prior to laboratory analysis. Four additional sediment samples were collected to constrain the maximum depositional age of the debris using infrared-stimulated luminescence dating from the unweathered debris beneath three soil profiles.

2.1 Structure from Motion photogrammetry

Structure from Motion photogrammetry is an efficient range-imaging technique for creating digital elevation models (DEMs) from spatially referenced photographs with a higher resolution than is often available from traditional remote sensing techniques (Johnson et al., 2014), including the 10 m DEM currently available from the 1/3 arcsecond US National Elevation Dataset. Photographs were taken during cloudless weather in January 2015 with a Nikon D610 camera using a fixed 85 mm lens. Camera

positions were georeferenced with a Trimble Juno ST handheld GPS unit (± 7 m accuracy). We used Agisoft Photoscan Pro, a commercial photogrammetric software package, to align 143 georeferenced photographs and generate a surface mesh. We exported a ~1 m spatial resolution DEM for subsequent morphometric analysis with the spatial analyst toolbox in ESRI ArcMap.

2.2 Laboratory soil analyses

Soil texture was measured in the laboratory using the hydrometer method of Gee and Bauder (1986). Soil color was determined for moist and dry soil samples by visual comparison to a Munsell® Soil Color Chart.

Mineralogical analysis of extracted, clay-sized particle fractions was performed using x-ray diffraction (XRD) analysis on smeared glass slides. To prepare for XRD, clay fractions were isolated by centrifugation, following dispersion of the soil in 100 mL of 5% sodium hexametaphosphate solution and agitation in a blender for three minutes. Extracted clay samples were then purified using mild (< pH 9.5) sodium hypochlorite to remove organics, and using citrate-dithionite buffer solution to remove short-order oxides (Soukup, 2008). To confirm lattice behavior in response to ion saturation and heat treatments, samples were first subdivided for ion-saturation in 1N $MgCl_2$ and 1N KCl. Following an initial XRD analysis, the Mg-saturated samples were exposed to ethylene glycol (EG) in a sealed desiccator for 48 hours and re-scanned. Three XRD scans were performed for the K-saturated samples. A first scan was performed on the unheated sample, a second scan after heating the sample to 350°C for four hours, and a third scan after heating the sample to 550°C for four hours (e.g., (Poppe et al., 2001).

Analyses were conducted on a Rigaku Ultima IV XRD spectrometer at the Pomona College Geology Department using Cu Kα radiation for continuous ~15 minute flat-stage scans from 4 to 30° 2θ at 40 kV and 44 mA. A sample of Clay Minerals Society reference standard PFI-1 containing palygorskite and smectite was treated and analyzed alongside field samples for verification of successfully induced Mg, K, EG, and heat effects. Mineral interpretations were made via comparison to the ICDD PDF-2 database (ICDD, 2003) and to other references (e.g. Dixon et al., 1990; Moore and Reynolds, 1997; Poppe et al., 2001) using Materials Data Jade 8 software.

Major and trace element concentrations were determined by fused glass bead X-ray fluorescence (XRF) spectrometry for sieved bulk soil samples and also for individual clasts from parent material. Powders of soil and clast samples were prepared in a Rocklabs® tungsten carbide head and mill. Powdered sample was mixed in a 1:2 ratio with a dilithium tetraborate flux, blended in a vortexer and fused to a glass bead in a graphite crucible at 1000°C for 15 minutes to one hour. Initial glass beads were then powdered and re-fused to ensure complete sample homogenization. Secondary beads were polished to a mirror finish and analyzed with a 3.0 kW Panalytical Axios wavelength dispersive XRF spectrometer in the Pomona College Geology Department following methodology adapted from Johnson et al. (1999). Elemental concentrations were compared to certified standardized reference materials (e.g. Lackey et al., 2012) and adjusted for loss-on-ignition.

2.3 Post-IR IRSL dating

Luminescence dating measures the time elapsed since sediment grains were last exposed to light. In many depositional environments, especially those where the transport distance is short, a significant portion of grains may not be exposed to light for long enough to reduce their initial luminescence signal to zero (Wallinga, 2008; McGuire and Rhodes, 2015). Single grain measurements provide a distribution of ages that can be analyzed statistically to identify the minimum value corresponding to the depositional age of sedimentary deposits (Rhodes, 2015). In this study we use infrared stimulated luminescence (IRSL) of single-grains of K-feldspar using a post-IR-IRSL protocol (Buylaert et al., 2009; Brown et al., 2015) , which has been demonstrated to agree well with age-controlled samples (Rhodes, 2015).

Samples were collected from sandy layers of bedded fluvial and colluvial sediments and stored in steel tubes in the field. Gamma ray spectrometer measurements were conducted at the sample locations to determine the gamma dose rate contribution from sediment at the sample location. Samples were subsequently processed under light controlled conditions at the University of California, Los Angeles. Samples were wet-sieved to separate the 175-200 μm fraction and K-feldspar grains were separated by density using the lighter separate from a lithium metatungstate heavy liquid with density 2.565 g/cm^3. Potassium-feldspar grains were then etched for 10 minutes in 10% HF to expose fresh mineral surfaces. For each sample, single K-feldspar grains were analyzed with a Riso TA-DA-20D TL/OSL reader. Individual grains were stimulated with infrared laser using a post-IR protocol detailed in the Supplementary Material (Buylaert et al., 2009; Fu et al., 2012) and luminescence emission was measured using BG3-BG39 filter combination in a 340 – 470 nm

transmission window. The depositional age is calculated using the methods outlined in Rhodes (2015). The average equivalent dose, dose rate and age is shown for each sample in Table 1. Additional details about the age calculation can be found in the Supplementary Material.

3. Results

3.1 Deposit morphology and sedimentology

Slope analysis of our ~1 m structure-from-motion DEM reveals a partially dissected planar surface extending 1.2 km into Cow Canyon (Figure 4). The surface dips 13° to the southwest with only 1.4 m average deviation in elevation from a planar surface fit. Complimentary slope analysis from coarser 10 m National Elevation Dataset confirms that additional Cow Canyon deposits have similar slopes (10-19° dip to the southwest) consistent with an interpretation that these deposits are relicts from a previous valley fill. All three surfaces project upstream to additional landslide debris that forms the low saddle drainage divide (Morton and Miller, 2003).

Deposits are poorly consolidated and thicken from less than 5 m to over 10 m with distance down the deposit surface from the surface apex, occasionally observed above a sharp bedrock contact. At the top of the deposit, poorly sorted angular clasts up to ~0.5 m diameter form a loose, matrix supported breccia. However, clast angularity decreases and the frequency of clast-supported layers increases with distance down the deposit. Lower elevation exposures display evidence of reworking, including crudely sorted layers of subrounded gravel and cobbles with finer-grained sand and silt lenses. Throughout the deposit, clasts are dominated by locally-sourced lithologies including vein quartz, andesite, basalt, granodiorite, amphibolite, micaceous pegmatite and

various gneisses, and the variability in clast lithology increases at lower elevation exposures. Clasts of the distinctive Pelona Schist were not observed.

3.2 Soil analyses

Field description. Soil profiles lack clearly illuviated B horizons, with darkened A horizons above pale AC and C horizons (Table 2 and Figure 5). Depth to the AC or C horizon ranges from 40 cm to 70 cm and horizon boundaries may be gradual or clear, smooth to wavy. All horizons generally exhibit angular to subangular blocky structure with very fine to very coarse pores and roots, and there are no systematic trends in soil structure, vegetation or porosity across the surface. Residual gravel fraction is typically <10% in the A horizon, increasing to 30-75% in the C horizon. The lowest elevation profile has an anomalously high (~33%) residual gravel fraction in the A horizon. Full field descriptions and photographs of soil profiles are provided in the Supplementary Material.

Texture and color. Soil texture ranges from loamy coarse sand to sandy clay loam (Table 2 and Figure 5). Sand content increases with depth in each profile and with decreasing surface elevation in A and C horizon. The two highest elevation profiles exhibited browner, darker dry soil color with A horizons of 7.5 YR 3/4 and 10 YR 4/4 compared to 7.5 YR 5/4 and 10 YR 5/4 at lower elevation profiles. Similarly, C horizons are 7.5 YR 4/6 in higher elevation profiles but 10 YR 6/4 and 10 YR 5/6 in lower elevation profiles.

In terms of master horizon type, texture, and thickness, soils most closely match a Haploxeroll description. However, the high color values and chromas of moist soil and

low organic matter content fail to satisfy the requirement for a mollic epipedon. Instead, we prefer classification of these soils as Typic Xerorthents which may be an intermediate match to the Hanford Series and the Shortcut Series, both considered minor components of Soil Survey Unit 316 (Soil Survey Staff, 2014).

Clay mineralogy. Clay-sized particle mineralogy indicates incipient soil profile development consistent with the Typic Xerothent subgroup of Entisols, or with very weak Inceptisols. Broad diffraction peaks indicate the presence of several distinct phyllosilicates in the clay-size particle fraction. These are predominately kaolin group clays, illite group clays, vermiculite, and trace smectite with clay-sized quartz also common (Table 2). Mica group diffraction peaks were weak in most samples despite the presence of visible and abundant mica flakes in field exposures of soil and bedrock clasts in parent material. This may be attributed to the large size of lithogenic mica grains which would not have been separated within the clay-sized particle class extracted for XRD analysis (detailed XRD data and mineralogical interpretations are available in the Supplemental Material). With the exception of the lowest elevation sample, clay mineralogy was similar between horizons of each profile, and between profile sites despite changes in total counts or in relative peak intensity. Samples from the lowest elevation profile showed the greatest mineralogical change within profile. The variety of clay minerals present and the lack of differentiation within this profile suggests incomplete chemical alteration of the lithogenic phyllosilicate mineral fraction.

Chemical weathering indices. Immobile element concentrations in parent material and soil can be used to evaluate the degree of chemical mass loss through weathering (Riebe et al., 2001). Following the approach of Muir and Logan (1982), we

used XRF analytical data to calculate *τ*, element loss relative to the concentration of an immobile element (e.g. Zr or Ti) in the unaltered parent material for each major element *i,* in the soil horizon *z*,

$$\tau_{i,z} = \left(\frac{i_z * Zr_{PM}}{i_{PM} * Zr_z} - 1\right) \quad (1)$$

where i_z and Zr_z are the concentration of element *i* and zirconium in soil horizon *z,* i_{PM} and Zr_{PM} are the concentration of element *i* and zirconium in the unaltered parent material. We also calculated the Chemical Depletion Fraction or CDF, as the total elemental loss in each soil horizon *z,* defined by (Riebe et al., 2001) as

$$\mathrm{CDF}_z = (1 - \frac{Zr_{PM}}{Zr_z}) \quad (2)$$

where notation follows from equation 1.

The concentration of immobile Zr and Ti increases from the debris parent material to the uppermost A horizon in each soil profile (Figure 6A). Nearly all measurements from soil profiles in Cow Canyon exhibit higher concentrations of immobile elements than published values from soils developed on bedrock in the eastern San Gabriel Mountains (Dixon et al., 2012), which may be explained by significant variability in bedrock mineralogy and enhanced weathering of debris soils. Debris soils show no evidence of significant accumulation of dust bearing the chemical signature of local dust inputs (Reheis and Kihl, 1995) complicating geochemical interpretations of bedrock soil development (Ferrier et al., 2011; Dixon et al., 2012).

Because the parent material of debris soils contains debris of heterogeneous composition, we compared Zr and Ti measurements in unweathered debris matrix sieved < 2 mm with nine individual debris clasts, chosen to represent the observed variability in local source rock lithology and pre-depositional weathering. There is no significant difference between the Zr/Ti ratio of sieved debris and the average of individual clast analyses, indicating that sieving debris < 2 mm effectively averages over any geochemical heterogeneity arising from source rock lithology and pre-depositional weathering (see figure in Supplemental Material). Additionally, though our relatively small sample size (n=4) of soil pits may fail to capture the variability of Zr concentrations in both parent material and mobile soil (Heimsath and Burke, 2013), our use of well-mixed debris as parent material should effectively homogenize any local variability in Zr arising from bedrock lithology.

Consistent with the weathering enrichment of immobile elements, elemental losses (i.e. τ_i) and CDF values are greatest in all soil profile A horizons (Table 3). On average, soils developed on landslide debris exhibit greater CDF values than bedrock soils (Dixon et al., 2012) and greater elemental loss (τ_i is more negative with greater elemental loss) in all major elements except K (Figure 6B). Elemental losses are greatest in the middle-elevation profiles B and C for all elements except Fe, and profile B exhibits the highest CDF and greatest elemental loss values negative tau values for each element. While there is no systematic relationship between elemental loss and soil texture or color, the sandy lowest elevation profile (profile D, with ~33% residual gravel in the A horizon and 60.8% sand in sieved material) also exhibits the lowest CDF values.

3.3 Post-IR IRSL dating

All four luminescence samples are consistent with deposition in the late Pleistocene (Table 1). The dates show two distinct populations at ~40 ka (41.0 ± 2.3 ka, 39.0 ± 2.1 ka) and ~33 ka (33.9 ± 1.9 ka and 32.3 /- 1.6 ka) depositional age. Luminescence dates of sedimentary deposits can overestimate depositional ages due to incomplete zeroing of the signal before deposition, an effect known as partial bleaching. Partial bleaching can be particularly problematic in steep-slope catchments proximal to headwaters (Kars et al., 2014; McGuire and Rhodes, 2015). The details of our statistical model to identify a minimum equivalent dose for the age calculation are given in the Supplemental Material.

4. Discussion

We interpret the deposits in Cow Canyon to represent relict fragments of a larger, more extensive valley fill surface. Deposits exhibit much lower slopes than expected for colluvium near the angle-of-repose (~37° in the San Gabriel Mountains, DiBiase et al., 2012) but are well explained by a continuous, low-sloping debris apron extending across the valley. Extrapolation of deposit surfaces across Cow Canyon would encompass 3.6-5.8 km^2 or 30-60% of the current catchment area, totaling an estimated 0.2-0.6 km^3 of fill in the present day canyon.

Debris aprons and cones may form from the wet remobilization of colluvium by debris flows with short runouts (e.g. Brazier et al., 1988) and our observations of crude sorting, fine-sediment lenses and progressive downslope clast rounding support

reworking by debris flows, a process common in the San Gabriel Moutnains (e.g. Lavé and Burbank, 2004). Observations of angular, poorly sorted and matrix-supported material near the apex of deposit surfaces may instead by explained by direct deposition of colluvial debris from adjacent hillslopes by dry ravel (Lamb et al., 2013).

Luminescence dating constrains a maximum ~40 ka depositional age for these deposits, with two ~33 ka ages possibly indicating a period of debris reworking. These depositional ages significantly precede aggradation along the North Fork of San Gabriel River, where radiocarbon (Bull, 1991), luminescence and cosmogenic exposure dating (Scherler et al., 2016) constrain an earliest deposition period of ~8-9 ka. According to the landslide frequency-magnitude relationship developed for the San Gabriel Mountains by Lave and Burbank (2004), a ~40 ka depositional age exceeds the recurrence interval for even the largest landslide events, and broadly suggests that landslide debris may be stored over 10^4 yr timescales. The potential for subsequent reworking of this landslide debris throughout the downstream San Gabriel River system indicates that landslide debris may be a persistent source of chemical solute in this rapidly eroding landscape.

4.1 Storage of landslide debris in Cow Canyon

We interpret that aggradation of Cow Canyon resulted from mobilization of a local debris source and does not necessarily implicate a climatically-driven change in hillslope debris flux (e.g. Bull, 1990) or late Pleistocene river reorganization (e.g. Morton et al., 1989). While at least three discrete strands of the San Gabriel Fault Zone pass near the outlet from Cow Canyon (Dibblee and Minch, 2002; Morton and Miller, 2006),

this fault is interpreted to have been inactive throughout the Quaternary (Powell, 1993; Morton and Miller, 2003) and so tectonic damming is not presently considered as an alternative aggradation mechanism. However, fault strands may provide preexisting planes of weakness that promote landsliding along the northern margin of Cow Canyon.

Bull (1990) interpreted aggradation along the North Fork of the San Gabriel River as evidence for climatically-modulated changes in hillslope debris flux. Reinterpretation of these deposits by Scherler et al. (2016) instead suggests that valley aggradation is better explained by remobilization of landslide debris. Landslide debris may abruptly change sediment supply, locally aggradating portions of a preexisting river systems (Korup, 2005; Korup et al., 2010). In constrast, a climatic-modulated change in hillslope debris flux should be regionally extensive. Without documentation of contemporaneous deposits in adjacent river drainages, we consider the aggradation of Cow Canyon to reflect local reworking of landslide debris in a similar fashion as has been reported by Scherler et al. (2016). Further analysis of Quaternary deposits throughout the San Gabriel Mountains will continue to test this hypothesis.

Several studies have suggested that the upper portion of San Antonio Canyon originally drained through Cow Canyon to the East Fork of the San Gabriel River (e.g. Ehlig, 1958; Morton et al., 1989). Cow Canyon exhibits an anomalously low channel gradient, more consistent with a large upstream drainage area in the headwaters of San Antonio Canyon. Morton et al. (1989) suggest that the landslide deposit at the present drainage divide dammed the upper portion of San Antonio Canyon and headward erosion of a rangefront tributary captured this drainage area to form the modern drainage configuration. While reworked debris from this landslide may have contributed

to aggradation in the beheaded Cow Canyon, our observation of locally sourced clast lithologies in Cow Canyon deposits, as well as a lack of a diagnostic step in the upstream San Antonio Canyon channel steepness (Morton et al. 1989), suggest that the landslide deposits presently dividing San Antonio Canyon from Cow Canyon are not directly related to the ~33-40 ka debris we investigated, and could instead be filling a preexisting wind gap (e.g. Ehlig, 1958).

4.2 Weathering of landslide debris

We quantitatively explore the significance of landslide debris weathering by predicting the flux of chemical solute from generic bedrock and debris soils. We predict solute flux as a function of soil age, or the time since the establishment of a stable geomorphic surface, following the approach of Yoo and Mudd (2008) to estimate the solute flux from five mineral species using a linear dissolution rate (e.g. Hodson and Langan, 1999; White and Brantley, 2003) and a time-dependent decay coefficient. We assume the depth of a soil profile develops as an exponential function (Heimsath et al., 1997) where maximum sediment production and pedogenic rates are higher for bedrock soils forming on steep hillslopes than debris soils forming on lower-sloping deposit surfaces (Heimsath et al., 2012). We assume that parent material for both soils begins with a granodioritic composition consistent with average values of San Gabriel Mountain bedrock (Barth, 1990; Dixon et al., 2012). Since the porosity of parent material is unconstrained, we explore porosity values for landslide debris between a 0 (i.e. bedrock porosity value) and 0.4 (i.e. soil porosity value) volumetric fraction. Our modeling does not consider short-term effects from anthropogenic perturbations to the landscape (e.g.

deforestation/reforestation), which is an important consideration for very recent deposits in this landscape. See the Supplementary Material for a brief description of model parameters and implementation.

In both generic bedrock and debris soils, solute flux is maximized over an intermediate soil age. Low-sloping surfaces initially allow water to percolate and react, but pedogenesis eventually slows as the soil profile thickens and the supply of fresh minerals is depleted (Ferrier and Kirchner, 2008). Because the fresh mineral supply and thus rates of surface mineral weathering are assumed to be lower on low-sloping debris surfaces than steep bedrock hillslopes, the solute flux from thick, stable debris soils lags that of bedrock soils (Figure 7A). The solute flux from debris soils increases with the assumed initial volumetric porosity of parent debris, reducing the critical soil age over which the solute flux from both soils is equal (a solute flux ratio of 1). Assuming a characteristic bedrock soil age of 350 yr (the time necessary to erode the average bedrock soil thickness reported in Dixon et al. (2012) at an average erosion rate of 500 m/Ma), our modeling illustrates that the solute flux from debris soils may actually exceed that from bedrock soils when the porosity of parent debris exceeds a volumetric fraction of 0.25 (almost 50% that of the resulting soil porosity), and debris soil age ranges between ~10^2-10^3 yr.

While we do not constrain the age of soils forming on landslide debris in Cow Canyon directly, comparison of our soil profiles to regional chronosequences (Weldon and Sieh, 1980; McFadden, 1982; Bull, 1991) suggests that the debris soils in Cow Canyon are considerably younger than the ~33-40 ka depositional age of their parent material. Specifically, the absence of a clearly illuviated B horizon in relatively shallow

profiles (typically <1 m in depth) suggest a mid-late Holocene (1-4 ka) soil age. Moreover, soil depth and CDF measurements are consistent with model predictions from mid-late Holocene soil age (Figure 8). An apparent ~10x difference between soil and depositional ages for deposits in Cow Canyon may be strong evidence for frequent soil stripping in response to wildfire, strong precipitation events, or other processes. Indeed, the dynamics of soil erosion on a planar slope may be quite different from the diffusive transport processes assumed in the conceptual framework of our analytical model, and our modeling of generic soils should be viewed as generally illustrative rather than predictive of our specific study area. Moreover, the model parameter θ is useful to characterize volumetric porosity, but does not take into account pore size or geometry.

If debris soils date to ~1-4 ka, then we expect the solute flux from debris soil weathering is unlikely to have exceeded that from bedrock soils in Cow Canyon. While this calculation remains sensitive to assumed maximum solute production rates, we propose that the broader interpretation of limited solute fluxes from debris soils is robust when debris soil age is more than 5x greater than bedrock soil age. Still, we conclude that landslide debris storage is an important supplementary source of chemical solute worthy of consideration in predictive modeling.

4.3 The contribution of landsliding to mountain weathering

While previous research has highlighted the role of landsliding on stream organization and sediment flux (e.g. Korup, 2004; Ouimet et al., 2008), the specific impact of landsliding on the solute flux of mountain landscapes has been only recently

explored. For example, Jin et al. (2016) observed elevated river solute fluxes following widespread landsliding during the Wenchuan earthquake of 2008. Elevated solute fluxes were linked to recent landsliding in both the Southern Alps (Emberson et al., 2015) and southern Taiwan (Emberson et al., 2016); both studies found the effect of landslides on solute fluxes dampened on decadal timescales.

Landsliding may directly, but temporarily (i.e. < 10^2 yr) enhance river solute fluxes by exposing fractured saprolite and bedrock, promoting weathering reactions at greater depth below the soil interface (Brantley et al., 2013; Riebe et al., 2016). Our observations further suggest that landsliding may also have an indirect, but lasting influence on solute fluxes by creating low-sloping surfaces that provide stable sites and a high surface-area substrate for soil development in otherwise unstable landscapes. This may occur through reworking of landslide debris into shallow, planar surfaces by dry or wet colluvial processes or as mountain rivers rework and abandon landslide debris (Ouimet et al., 2007; Yanites et al., 2010; Scherler et al., 2016). The importance of weathering of landslide debris will depend on the timescale of mineral depletion and debris removal, the latter of which is a balance between the frequency of mass wasting events and the transport capacity of the fluvial network (Emberson et al., 2016).

If landsliding is the dominant process restricting the development of a continuous soil cover in steep, rapidly eroding mountain landscapes (DiBiase et al., 2012; Larsen et al., 2014a), then we expect the contribution of landsliding to the landscape solute flux will be greatest in such bedrock-dominated landscapes and partially explain global observations of high solute fluxes from rapidly eroding landscapes (Larsen et al., 2014b).

5. Conclusion

In this study, we evaluate how weathering of stored landslide debris may supplement the chemical solute flux from bedrock-dominated landscapes. We present new measurements of surface and soil morphology, soil geochemistry, and luminescence-based depositional ages for landslide debris deposits in Cow Canyon, a tributary to the East Fork of the San Gabriel River in the eastern San Gabriel Mountains of California. The preservation of older landslide deposits provides the unique opportunity to study the temporal evolution of chemical weathering fluxes in a landscape with frequent landsliding but few relict surfaces. Reworking of landslide debris by dry colluvial and debris flow processes form low-sloping surfaces that host relatively young, but developing, oxidized, soils in an otherwise unstable, bedrock-dominated landscape rapidly eroding by landsliding. Luminescence depositional age dating indicates that landslide debris may be stored over 10^4 timescales, significantly longer than the longest recurrence estimates of large landslide events in the San Gabriel Mountains. If landslide debris is a persistent feature of this landscape, pedogenesis on low-sloping, stable deposit surfaces will supplement, but likely not surpass, the solute flux of these rapidly eroding landscapes. Broadly, we conclude that landslide debris storage may be an important supplementary source of chemical solute, but is unlikely to dominate the chemical solute flux of rapidly eroding, bedrock-dominated landscapes. More study is necessary to constrain the spatial variability in soil properties across these unusual preserved surfaces; this study could be repeated at other large landslide deposits in the San Gabriel Mountains, such as at Crystal Lake, to better understand how debris age

and geomorphic context affect soil formation. Locally, however, the persistence of chemical weathering in steep, bedrock-dominated landscapes that primarily erode by processes of mass wasting, yields unique pedogenic and sedimentary environments that bear further consideration in the evolving view of debris storage and solute flux in mountain landscapes.

Acknowledgements

We acknowledge support from Pomona College and a Sigma Xi Grant-in-aid to JD. JD designed the research with KAL and CRR. CM and ER conducted luminescence analyses. All authors contributed to field work and writing the manuscript. We thank J. Dixon, K. Ferrier and R. Hazlett for productive discussions and the USFS Angeles National Forest staff for granting access to field sites and permission to collect samples. We thank Jonathan Harris and Sarah Granke for lab support. We thank one anonymous reviewer and Arjun Heimsath for constructive reviews and Fiona Kirkby for editorial support.

References

Anderson, S.W., Anderson, S.P., and Anderson, R.S., 2015, Exhumation by debris flows in the 2013 Colorado Front Range storm: Geology, v. 43, no. 5, p. 391–394, doi: 10.1130/G36507.1.

Berner, R.A., 1991, A model for atmospheric CO 2 over Phanerozoic time: American Journal of Science, v. 291, no. 4, p. 339–376, doi: 10.2475/ajs.291.4.339.

Binnie, S.A., Phillips, W.M., Summerfield, M.A., and Fifield, L.K., 2007, Tectonic uplift,

threshold hillslopes, and denudation rates in a developing mountain range: Geology, v. 35, no. 8, p. 743, doi: 10.1130/G23641A.1.

Barth, A.P., 1990, Mid-crustal emplacement of Mesozoic plutons, San Gabriel Mountains, California, and implications for the geologic history, *in* The nature and origin of Cordilleran magmatism, Geological Society of America.

Berner, R.A., Univ., R.A. (Yale, Haven, N., and States)), C. (United, 1991, A model for atmospheric CO 2 over Phanerozoic time: American Journal of Science, v. 291, no. 4, p. 339–376, doi: 10.2475/ajs.291.4.339.

Bluth, G.J.S., and Kump, L.R., 1994, Lithologic and climatologic controls of river chemistry: Geochimica et Cosmochimica Acta, v. 58, no. 10, p. 2341–2359.

Blythe, A., 2002, Low-temperature thermochonology of the San Gabriel and San Bernardino Mountains, Southern California; constraining structural evolution: Geological Society of America Special Papers, v. 365, p. 231–250.

Brantley, S.L., Holleran, M.E., Jin, L., and Bazilevskaya, E., 2013, Probing deep weathering in the Shale Hills Critical Zone Observatory, Pennsylvania (USA): The hypothesis of nested chemical reaction fronts in the subsurface: Earth Surface Processes and Landforms, v. 38, no. 11, p. 1280–1298, doi: 10.1002/esp.3415.

Brazier, V., Whittington, G., and Ballantyne, C.K., 1988, Holocene debris cone evolution in Glen Etive, Western Grampian Highlands, Scotland: Earth Surface Processes and Landforms, v. 13, no. 6, p. 525–531, doi: 10.1002/esp.3290130606.

Brown, N.D., Rhodes, E.J., Antinao, J.L., and McDonald, E.V., 2015, Single-grain post-IR IRSL signals of K-feldspars from alluvial fan deposits in Baja California Sur,

Mexico: Quaternary International, v. 362, p. 132–138, doi: 10.1016/J.QUAINT.2014.10.024.

Bull, W.B., 1991, Geomorphic Responses to Climate Change: Oxford University Press, London.

Bull, W.B., 1990, Stream-terrace genesis: implications for soil development: Geomorphology, v. 3, no. 3–4, p. 351–367.

Buylaert, J.P., Murray, A.S., and Thomsen, K.J., 2009, Testing the potential of an elevated temperature IRSL signal from K-feldspar: Radiation Measurements, v. 44, no. 5, p. 560–565, doi: 10.1016/j.radmeas.2009.02.007.

Chamberlin, T.C., 1899, An attempt to frame a working hypothesis of the cause of glacial periods on an atmospheric basis: Journal of Geology, v. 7, p. 545–584.

Crowell, J.C., 1982, The tectonics of Ridge Basin, southern California, *in* Geologic History of Ridge Basin, Southern California, p. 25–42.

Dibblee, T.W., and Minch, J.A., 2002, Geologic map of the Mount Baldy Quadrangle, Los Angeles and San Bernardino Counties, California:

DiBiase, R.A., Heimsath, A.M., and Whipple, K.X., 2012, Hillslope response to tectonic forcing in threshold landscapes: Earth Surface Processes and Landforms, v. 37, no. 8, p. 855–865.

DiBiase, R.A., Whipple, K.X., Heimsath, A.M., and Ouimet, W.B., 2010, Landscape form and millennial erosion rates in the San Gabriel Mountains, CA: Earth and Planetary Science Letters, v. 289, no. 1–2, p. 134–144.

Dixon, J.L., Hartshorn, A.S., Heimsath, A.M., DiBiase, R.A., and Whipple, K.X., 2012,

Chemical weathering response to tectonic forcing: A soils perspective from the San Gabriel Mountains, California: Earth and Planetary Science Letters, v. 323–324, p. 40–49.

Dixon, J.B., Weed, S.B., and PARPITT, R.L., 1990, Minerals in Soil Environments: Soil Science, v. 150, no. 2, p. 562, doi: 10.1097/00010694-199008000-00011.

Dolan, J.F., Gath, E.M., Grant, L.B., Legg, M., Lindvall, S., Mueller, K., Oskin, M., Ponti, D.F., Rubin, C.M., Rockwell, T.K., John, H., Treiman, a, Walls, C., and Yeats, R.S., 1996, Active Faults in the Los Angeles Metropolitan Region: , no. 1, p. 1–47.

Ehlig, P.L., 1958, The Geology of the Mount Baldy Region of the San Gabriel Mountains, California: University of California, Los Angeles, 200 p.

Emberson, R., Hovius, N., Galy, A., and Marc, O., 2015, Chemical weathering in active mountain belts controlled by stochastic bedrock landsliding: Nature Geoscience, v. 2, no. November, doi: 10.1038/ngeo2600.

Emberson, R., Hovius, N., Galy, A., and Marc, O., 2016, Oxidation of sulfides and rapid weathering in recent landslides: Earth Surface Dynamics, v. 4, no. 3, p. 727–742, doi: 10.5194/esurf-4-727-2016.

Ferrier, K.L., and Kirchner, J.W., 2008, Effects of physical erosion on chemical denudation rates: A numerical modeling study of soil-mantled hillslopes: Earth and Planetary Science Letters, v. 272, no. 3–4, p. 591–599, doi: 10.1016/j.epsl.2008.05.024.

Ferrier, K.L., Kirchner, J.W., and Finkel, R.C., 2011, Estimating millennial-scale rates of dust incorporation into eroding hillslope regolith using cosmogenic nuclides and

immobile weathering tracers: Journal of Geophysical Research: Earth Surface, v. 116, p. 1–11, doi: 10.1029/2011JF001991.

Fu, X., Li, B., and Li, S.-H., 2012, Testing a multi-step post-IR IRSL dating method using polymineral fine grains from Chinese loess: Quaternary Geochronology, v. 10, p. 8–15, doi: 10.1016/J.QUAGEO.2011.12.004.

Gabet, E.J., and Mudd, S.M., 2009, A theoretical model coupling chemical weathering rates with denudation rates: Geology, v. 37, no. 2, p. 151–154, doi: 10.1130/G25270A.1.

Gee, G.W., and Bauder, J.W., 1986, Particle-size analysis, *in* Methods of soil analysis, Part 1: Physical and mineralogical methods, Agronomy Monograph 9, p. 383–411.

Godsey, S.E., Kirchner, J.W., and Clow, D.W., 2009, Concentration-discharge relationships reflect chemostatic characteristics of US catchments: Hydrological Processes, v. 23, p. 1844–1864, doi: 10.1002/hyp.

Heimsath, A.M., and Burke, B.C., 2013, The impact of local geochemical variability on quantifying hillslope soil production and chemical weathering: Geomorphology, v. 200, p. 75–88, doi: 10.1016/j.geomorph.2013.03.007.

Heimsath, A.M., DiBiase, R. a., and Whipple, K.X., 2012a, Soil production limits and the transition to bedrock-dominated landscapes: Nature Geoscience, v. 5, no. 3, p. 210–214, doi: 10.1038/ngeo1380.

Heimsath, A.M., DiBiase, R. a., and Whipple, K.X., 2012b, Soil production limits and the transition to bedrock-dominated landscapes: Nature Geoscience, v. 5, no. 3, p. 210–214, doi: 10.1038/ngeo1380.

673 Heimsath, A.M., Dietrich, W.E., Nishiizumi, K., and Finkel, R.C., 1997, The Soil
674 Production Function and Landscape Equilibrium: Nature, v. 388, no. 24, p. 358–
675 361, doi: 10.1144/SP312.8.

676 Hodson, M.E., and Langan, S.J., 1999, Considerations of uncertainty in setting critical
677 loads of acidity of soils: the role of weathering rate determination: Environmental
678 Pollution, v. 106, no. 1, p. 73–81, doi: 10.1016/S0269-7491(99)00058-5.

679 Hovius, N., Stark, C.P., and Allen, P.A., 1997, Sediment flux from a mountain belt
680 derived by landslide mapping: Geology, v. 25, no. 3, p. 231–234, doi:
681 10.1130/0091-7613(1997)025<0231:SFFAMB>2.3.CO;2.

682 Jin, Z., Joshua West, A., Zhang, F., An, Z., Hilton, R.G., Yu, J., Wang, J., Li, G., Deng,
683 L., and Wang, X., 2016, Seismically enhanced solute fluxes in the Yangtze River
684 headwaters following the A.D. 2008 Wenchuan earthquake: Geology, v. 44, no. 1,
685 p. 47–50, doi: 10.1130/G37246.1.

686 Johnson, D.M., Hooper, P.R., and Conrey, R.M., 1999, XRF analysis of rocks and
687 minerals for major and trace elements on a single low dilution Litetraborate fused
688 bead: Advances in X-Ray Analysis, v. 41, p. 843–867.

689 Johnson, K., Nissen, E., Saripalli, S., Arrowsmith, J.R., McGarey, P., Scharer, K.,
690 Williams, P., and Blisniuk, K., 2014, Rapid mapping of ultrafine fault zone
691 topography with structure from motion: Geosphere, v. 10, no. 5, p. 969–986, doi:
692 10.1130/GES01017.1.

693 Kars, R.H., Reimann, T., Ankjaergaard, C., and Wallinga, J., 2014, Bleaching of the
694 post-IR IRSL signal: new insights for feldspar luminescence dating: Boreas, v. 43,

no. 4, p. 780–791, doi: 10.1111/bor.12082.

Korup, O., 2005, Geomorphic imprint of landslides on alpine river systems, southwest New Zealand: Earth Surface Processes and Landforms, v. 30, no. 7, p. 783–800, doi: 10.1002/esp.1171.

Korup, O., 2004, Landslide-induced river channel avulsions in mountain catchments of southwest New Zealand: Geomorphology, v. 63, p. 57–80, doi: 10.1016/j.geomorph.2004.03.005.

Korup, O., Densmore, A.L., and Schlunegger, F., 2010, The role of landslides in mountain range evolution: Geomorphology, v. 120, no. 1–2, p. 77–90, doi: 10.1016/j.geomorph.2009.09.017.

Kump, L.R., Brantley, S.L., and Arthur, M.A., 2000, Chemical Weathering, Atmospheric CO2, and Climate: Annual Review of Earth and Planetary Sciences, v. 28, no. 1, p. 611–667, doi: 10.1146/annurev.earth.28.1.611.

Lackey, J.S., Cecil, M.R., Windham, C.J., Frazer, R.E., Bindeman, I.N., and Gehrels, G.E., 2012, Fine Gold Intrusive Suite: The roles of basement terranes and magma source development in the Early Cretaceous Sierra Nevada batholith: Geosphere, v. 8, no. 2, p. 292, doi: 10.1130/GES00745.1.

Lamb, M.P., Levina, M., DiBiase, R. a., and Fuller, B.M., 2013, Sediment storage by vegetation in steep bedrock landscapes: Theory, experiments, and implications for postfire sediment yield: Journal of Geophysical Research: Earth Surface, v. 118, no. 2, p. 1147–1160, doi: 10.1002/jgrf.20058.

Larsen, I.J., Almond, P.C., Eger, A., Stone, J.O., Montgomery, D.R., and Malcolm, B.,

2014a, Rapid Soil Production and Weathering in the Southern Alps, New Zealand: Science, v. 343, no. February, p. 637–641, doi: 10.1126/science.1244908.

Larsen, I.J., and Montgomery, D.R., 2012, Landslide erosion coupled to tectonics and river incision: Nature Geoscience, v. 5, no. 7, p. 468–473, doi: 10.1038/ngeo1479.

Larsen, I.J., Montgomery, D.R., and Greenberg, H.M., 2014b, The contribution of mountains to global denudation: Geology, v. 42, no. 6, p. 527–530, doi: 10.1130/G35136.1.

Lavé, J., and Burbank, D.W., 2004, Denudation processes and rates in the Transverse Ranges, southern California: Erosional response of a transitional landscape to external and anthropogenic forcing: Journal of Geophysical Research, v. 109, no. F1, p. F01006, doi: 10.1029/2003JF000023.

Maher, K., and Chamberlain, C.P., 2014, Hydrologic Regulation of Chemical Weathering and the Geologic Carbon Cycle: v. 1502, no. March, p. 1–4, doi: 10.1126/science.1250770.

McFadden, L.D., 1982, The Impacts of Temporal and Spatial Climatic Changes on Alluvial Soils Genesis in Southern Calfornia: The University of Arizona.

McGuire, C., and Rhodes, E.J., 2015, Downstream MET-IRSL single-grain distributions in the Mojave River, southern California: Testing assumptions of a virtual velocity model: Quaternary Geochronology, v. 30, p. 239–244, doi: 10.1016/j.quageo.2015.02.004.

Millot, R., Gaillardet, J., Dupré, B., and Allègre, C.J., 2002, The global control of silicate weathering rates and the coupling with physical erosion: new insights from rivers of

the Canadian Shield: Earth and Planetary Science Letters, v. 196, no. 1, p. 83–98, doi: 10.1016/S0012-821X(01)00599-4.

Montgomery, D.R., and Brandon, M.T., 2002, Topographic controls on erosion rates in tectonically active mountain ranges: Earth and Planetary Science Letters, v. 201, no. 3–4, p. 481–489, doi: 10.1016/S0012-821X(02)00725-2.

Moon, S., Page Chamberlain, C., Blisniuk, K., Levine, N., Rood, D.H., and Hilley, G.E., 2011, Climatic control of denudation in the deglaciated landscape of the Washington Cascades: Nature Geoscience, v. 4, no. 7, p. 469–473, doi: 10.1038/ngeo1159.

Moore, D.M., and Reynolds, R.C., 1997, X-ray Diffraction and the Identification and Analysis of Clay Minerals: Oxford University Press.

Morton, B.D.M., and Miller, F.K., 2003, Preliminary geologic map of the San Bernardino 30’ x 60’ quadrangle, California.:

Morton, D.M., Sadler, P.M., and Minnich, R.A., 1989, Large rock-avalanche deposits: examples from the central and eastern San Gabriel Mountains of Southern California: Publications of the Inland Geological Society, v. 2, p. 323–337.

Muir, J.W., and Logan, J., 1982, Eluvial/illuvial coefficients of major elements and the corre- sponding losses and gains in three soil profile: Journal of Soil Science, v. 32, no. 2, p. 295–308.

Niemi, N. a., Oskin, M., Burbank, D.W., Heimsath, A.M., and Gabet, E.J., 2005, Effects of bedrock landslides on cosmogenically determined erosion rates: Earth and Planetary Science Letters, v. 237, no. 3–4, p. 480–498, doi:

10.1016/j.epsl.2005.07.009.

Nourse, J., 2002, Miocene reconstruction of the central and eastern San Gabriel Mountains, southern California, with implications for evolution of the San Gabriel fault and Los Angeles: Geological Society of America, Special Paper, v. 365, p. 161–185.

Ouimet, W.B., Whipple, K.X., Crosby, B.T., Johnson, J.P., and Schildgen, T.F., 2008, Epigenetic gorges in fluvial landscapes: 2Earth Surface Processes and Landforms, v. 33, p. 1993–2009, doi: 10.1002/esp.1650 Epigenetic.

Ouimet, W.B., Whipple, K.X., Royden, L.H., Sun, Z., and Chen, Z., 2007, The influence of large landslides on river incision in a transient landscape: Eastern margin of the Tibetan Plateau (Sichuan, China): Bulletin of the Geological Society of America, v. 119, no. 11–12, p. 1462–1476, doi: 10.1130/B26136.1.

Poppe, L.J., Paskevich, V.F., Hathaway, J.C., and Blackwood, D.S., 2001, A laboratory manual for X-ray powder diffraction: , p. 1–88.

Powell, R.E., 1993, Chapter 1: Balanced palinspastic reconstruction of pre-late Cenozoic paleogeology, southern California: Geologic and kinematic constraints on evolution of the San Andreas fault system: Memoir of the Geological Society of America, v. 178, no. 1, p. 1–106, doi: 10.1130/MEM178-p1.

Raymo, M.E., and Ruddiman, W.F., 1992, Tectonic forcing of late Cenozoic climate: Nature, v. 359, no. 6391, p. 117–122, doi: 10.1038/359117a0.

Reheis, M.C., and Kihl, R., 1995, Dust deposition in southern Nevada and California, 1984-1989: relations to climate, source area, and source lithology: Journal of

Geophysical Research, v. 100, p. 8893–8918, doi: 10.1029/94JD03245.

Rhodes, E.J., 2015, Dating sediments using potassium feldspar single-grain IRSL: initial methodological considerations: Quaternary International2, v. 362, p. 14–22.

Riebe, C.S., Hahm, W.J., and Brantley, S.L., 2016, Controls on deep critical zone architecture: a historical review and four testable hypotheses: Earth Surface Processes and Landforms, doi: 10.1002/esp.4052.

Riebe, C.S., Kirchner, J.W., and Finkel, R.C., 2004, Erosional and climatic effects on long-term chemical weathering rates in granitic landscapes spanning diverse climate regimes: Earth and Planetary Science Letters, v. 224, p. 547–562, doi: 10.1016/j.epsl.2004.05.019.

Riebe, C.S., Kirchner, J.W., Granger, D.E., and Finkel, R.C., 2001, Strong tectonic and weak climatic control of long-term chemical weathering rates: Geology, v. 29, p. 511–514, doi: 10.1130/0091-7613(2001)029<0511:STAWCC>2.0.CO.

Roering, J.J., Perron, J.T., and Kirchner, J.W., 2007, Functional relationships between denudation and hillslope form and relief: Earth and Planetary Science Letters, v. 264, no. 1–2, p. 245–258, doi: 10.1016/j.epsl.2007.09.035.

Scherler, D., Lamb, M.P., Rhodes, E.J., and Avouac, J.P., 2016, Climate-change versus landslide origin of fill terraces in a rapidly eroding bedrock landscape: San Gabriel River, California: Bulletin of the Geological Society of America, v. 128, no. 7, p. 1228–1248, doi: 10.1130/B31356.1.

Schoeneberger, P.J., Wysocki, D.A., Benham, E.C., and Soil Survey Staff, 2012, Field Book for Describing and Sampling Soils: , no. September.

Soil Survey Staff, 2014, Soil Survey Field and Laboratory Methods Manual. Soil Survey Investigations Report No. 51, Version 2.0. R. Burt and Soil Survey Staff (ed.). U.S. Department of Agriculture, Natural Resources Conservation Service

Soukup, 2008, Preparing soils for mineralogical analysis, *in* Ulrey, A. and Drees, R. eds., SSSA Book Series No. 5, Soil Science Society of America, Madison, p. 13–31.

Spotila, J., and House, M., 2002, Controls on the erosion and geomorphic evolution of the San Bernardino and San Gabriel Mountains, southern California: Geological Society of America, Special Paper, v. 365, p. 205–230, doi: 10.1130/0-8137-2365-5.205.

Urey, H., 1952, The planets: their origin and development: Yale University Press: New Haven.

Walker, J.C.G., Hays, P.B., and Kasting, J.F., 1981, A negative feedback mechanism for the long-term stabilization of Earth's surface temperature: Journal of Geophysical Research, v. 86, no. C10, p. 9776, doi: 10.1029/JC086iC10p09776.

Wallinga, J., 2008, Optically stimulated luminescence dating of fluvial deposits: a review: Boreas, v. 31, no. 4, p. 303–322, doi: 10.1111/j.1502-3885.2002.tb01076.x.

Warrick, J.A., Milliman, J.D., Walling, D.E., Wasson, R.J., Syvitski, J.P.M., and Aalto, R.E., 2014, Earth is (mostly) flat: Apportionment of the flux of continental sediment over millennial time scales: COMMENT: Geology, v. 42, no. 1, p. e316–e316, doi: 10.1130/G34846C.1.

Weldon, R.J., and Sieh, K.E., 1985, Holocene rate of slip and tentative recurrence

interval for large earthquakes on the San Andreas fault in Cajon Pass, southern California: Geological Society of America Bulletin, v. 96, p. 793–812.

West, A.J., 2012, Thickness of the chemical weathering zone and implications for erosional and climatic drivers of weathering and for carbon-cycle feedbacks: Geology, v. 40, no. 9, p. 811–814, doi: 10.1130/G33041.1.

West, A.J., Galy, A., and Bickle, M., 2005, Tectonic and climatic controls on silicate weathering.:

Westoby, M.J., Brasington, J., Glasser, N.F., Hambrey, M.J., and Reynolds, J.M., 2012, "Structure-from-Motion" photogrammetry: A low-cost, effective tool for geoscience applications: Geomorphology, v. 179, p. 300–314, doi: 10.1016/j.geomorph.2012.08.021.

White, A.F., and Brantley, S.L., 2003, The effect of time on the weathering of silicate minerals: why do weathering rates differ in the laboratory and field? Chemical Geology, v. 202, no. 3, p. 479–506, doi: 10.1016/j.chemgeo.2003.03.001.

Willenbring, J.K., Codilean, A.T., and McElroy, B., 2013, Earth is (mostly) flat: Apportionment of the flux of continental sediment over millennial time scales: Geology, v. 41, no. 3, p. 343–346, doi: 10.1130/G33918.1.

Yanites, B.J., Tucker, G.E., Mueller, K.J., Chen, Y.G., Wilcox, T., Huang, S.Y., and Shi, K.W., 2010, Incision and channel morphology across active structures along the Peikang River, central Taiwan: Implications for the importance of channel width: Bulletin of the Geological Society of America, v. 122, no. 7–8, p. 1192–1208, doi: 10.1130/B30035.1.

Yerkes, R.F., Campbell, R.H., Alvarez, R.M., and Bovard, K.R., 2005, Preliminary geologic map of the Los Angeles 30′× 60′ Quadrangle, southern California.:

Yoo, K., and Mudd, S.M., 2008, Toward process-based modeling of geochemical soil formation across diverse landforms: A new mathematical framework: Geoderma, v. 146, no. 1, p. 248–260, doi: 10.1016/j.geoderma.2008.05.029.

Figure Captions

Figure 1: Analytical models of mineral weathering in a steady-state soil profile fail to explain observations of elevated solute fluxes in rapidly eroding landscapes where landsliding restricts the development of a continuous soil profile. For example, the solid line illustrates the predictive model of Gabet and Mudd (2009) using parameters derived for the San Gabriel Mountains. The dashed line illustrates a regression of global observations of physical and chemical denudation rates by Larsen et al. (2014). Mismatch at high erosion rates requires additional solute from alternative sources in the landscape, such as direct weathering of saprolite or stored debris. See Supplementary Material for model parameters.

Figure 2: Landslide debris is ubiquitous in the eastern San Gabriel Mountains. The San Gabriel Mountains comprise crystalline basement units exhumed along large, range-bounding thrust faults (thick white lines; SMFZ = Sierra Madre Fault Zone, CFZ = Cucamonga Fault Zone) in a restraining bend of the San Andreas Fault (SAF). Topographic relief increases from west to east across the mountains, and is highest in the vicinity of Mount San Antonio (B). Correspondingly, the extent of mapped landslide deposits (black areas, mapped by Yerkes and Campbell, 2005 and Morton and Miller, 2006) increases in eastern high relief catchments like the North Fork of the San Gabriel River (NF), San Antonio Canyon (SAC) and Cow Canyon (CC), shown in detail in Figure 3.

Figure 3: Landslide debris stored along the North Fork of the San Gabriel River (NF), Cow Canyon (CC) and San Antonio Canyon (SAC) forms low-sloping deposits above river channels that provide stable surfaces for pedogenesis in an otherwise unstable landscape. Landslide deposits mapped by Morton and Miller (2006) are represented by black hatching and hillslope angles are calculated from the 10 m digital elevation model from the US National Elevation Dataset. Inset box and camera icons respectively mark the extent of Figure 4 and location of featured field photographs.

Figure 4: A. Perspective views of surfaces in Cow Canyon from field photographs looking westward and northward show densely vegetated relict surfaces (black

hatching) from a larger valley fill. Location of photographs illustrated in Figure 3. B. High resolution (~1 m) slope map derived from Structure from Motion photogrammetry of the largest landslide debris surface reveals a partially dissected 1.2 km long planar surface dipping an average 13 degrees to the southwest. Four soil profiles were chosen to capture the full soil variability across the surface catena. The three highest elevation soil profiles (A, B and C) were described at the margin of the intact deposit surface while lowest elevation profile (D) was collected from a highly degraded portion of the deposit. Additional views of the deposits can be seen in Supplemental Figure 5.

Figure 5. Soils developed on Cow Canyon surfaces are thicker than bedrock soils reported from three sites in the eastern San Gabriel Mountains (data from Dixon et al. 2012; *n* is the number of soil depth measurements per site) and show weak horizonation, lacking clearly illuviated B horizons. Textual trends in each profile show a reduction in sand and increase in clay accumulation, possibly indicating accumulation of aerosolic dust and/or secondary weathering products. Color photographs of soil profiles are available in Supplementary Figures 5 through 8.

Figure 6: A. Weathering of debris parent material increases the concentration of immobile elements Zr and Ti between the C and A horizons of each soil profile (trends shown as black arrows). Compared to published values of bedrock soils from three locations in the eastern San Gabriel Mountains (grey arrows, Dixon et al. 2012), debris soils in Cow Canyon exhibit a greater degree of immobile element enrichment. Debris soils are apparently unbiased by dust accumulation from Mojave or San Gabriel Mountain sources (Reheis and Kihl, 1995). Bedrock soil elemental values are averages from multiple measurements at each site, showing one standard deviation.
B. Complimentary measurements of mobile element losses (τ values) demonstrate enhanced weathering of debris soils. Debris soils typically show more (i.e. more negative) losses than observations from the same bedrock soils in panel A. Accordingly, mean CDF values from debris soils exceed that of bedrock soils.

Figure 7: A. Following the approach of Yoo and Mudd (2008), we predict the solute flux from bedrock and debris soils as a function of their age. We assume rates of soil formation are lower on low sloping debris surfaces such that the solute flux from debris soils lags that of bedrock soils. The solute flux from debris soils strongly depends on initial debris porosity, shifting the age over which the solute flux from debris soils exceeds that of bedrock soils. See Supplementary Material for model details and parameters. B. Contour plot of predicted solute flux ratio between debris and bedrock soils. We illustrate that the solute flux from debris soils may exceed that from bedrock soils where initial debris porosity exceeds ~0.25 and debris soils age ranges between 10^2-10^3 yr.

Figure 8. Observations of soil thickness and CDF are consistent with a soil age ~1-4 ka, similar to regional chronosequence estimates of a mid-late Holocene age. Calculation assumes the same model of Yoo and Mudd (2008) used in Figure 7.

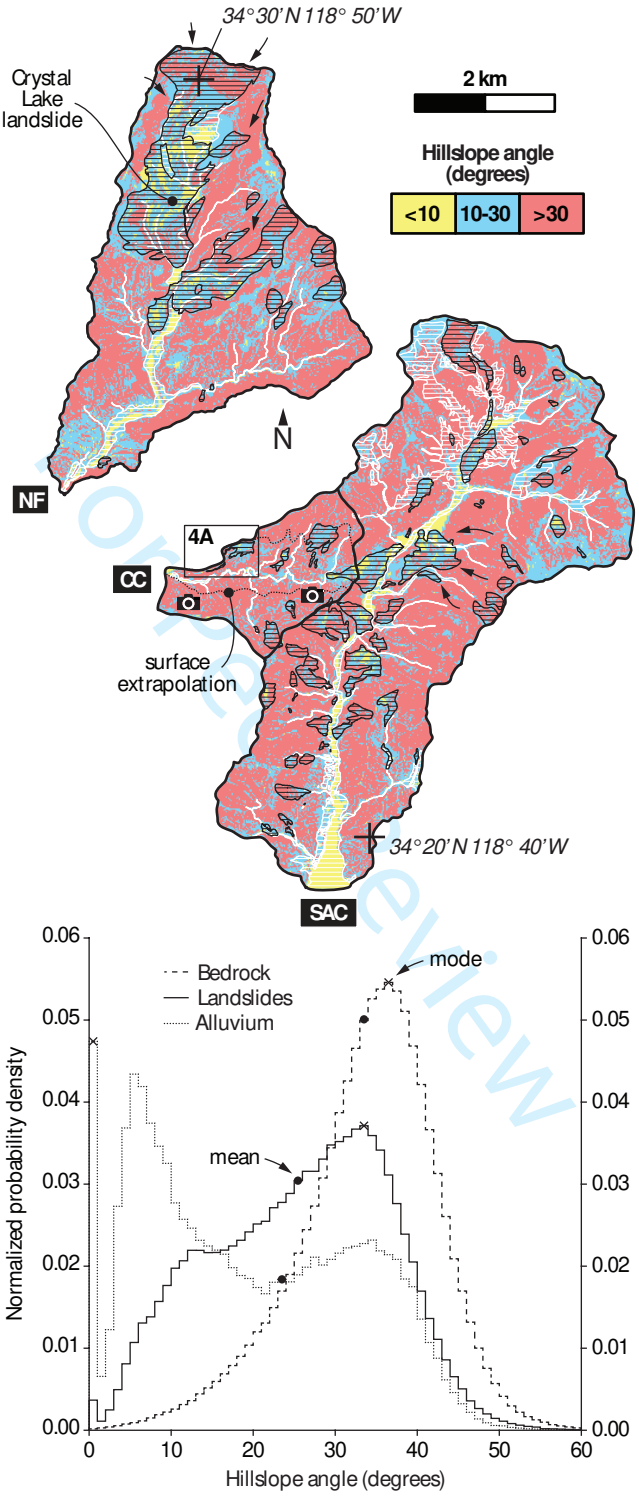

Table 1. Summary of soil profile observations (see Supplementary Material for detailed soil descriptions

Horizon	Munsell color (dry)	Texture			NRCS texture
		% Sand	% Silt	% Clay	
Profile A: 3788509E 435570N 1187 m elevation					
A (0-30 cm)	7.5YR 3/4	43.3	31.1	25.6	Loam
AC (30-62 cm)	7.5YR 5/6	48.3	30.2	21.5	Loam
C (62+ cm)	7.5YR 4/6	55.6	27.8	16.6	Fine Sandy Loam
Profile B: 3788450E 435315N 1136 m elevation					
A (0-20 cm)	10YR 4/4	55.5	31.8	12.7	Fine Sandy Loam
C1 (20-45 cm)	7.5YR 5/4	52.5	29.7	17.8	Fine Sandy Loam
2C2 (45-90+ cm)	7.5YR 4/6	64.4	20.5	15.0	Fine Sandy Loam
Profile C: 3788276E 435081N 1076 m elevation					
A (0-45 cm)	7.5Y4 5/4	49.6	25.6	24.8	Sandy Clay Loam
AC (45-70 cm)	7.5YR 6/6	52.8	35.6	11.5	Sandy Clay Loam
C (70+ cm)	10YR 6/4	72.4	18.9	8.6	Fine Sandy Loam
Profile D: 3788079E 434851N 1040 m elevation					
A (0-25 cm)	10YR 5/4	68.2	21.7	10.1	Sandy Loam
C1 (25-100 cm)	10YR 5/6	73.9	16.9	9.2	Sandy Loam
2C2 (100-130+ cm)	10YR 5/4	81.1	12.1	6.8	Loamy Coarse Sand

)

Clay-sized Particle Mineralogy (relative abundance)			
Kaolin Group	Vermiculite	Illite Group	Smectite Group
moderate (30-45%)	abundant (45-70%)	low (5-30%)	low (5-30%)
moderate (30-45%)	moderate (30-45%)	moderate (30-45%)	low (5-30%)
moderate (30-45%)	moderate (30-45%)	moderate (30-45%)	low (5-30%)
abundant (45-70%)	abundant (45-70%)	low (5-30%)	not detected
abundant (45-70%)	low (5-30%)	trace (< 5%)	not detected
predominant (>70%)	low (5-30%)	trace (< 5%)	trace (< 5%)
abundant (45-70%)	moderate (30-45%)	low (5-30%)	trace (< 5%)
abundant (45-70%)	abundant (45-70%)	low (5-30%)	trace (< 5%)
abundant (45-70%)	abundant (45-70%)	low (5-30%)	low (5-30%)
abundant (45-70%)	trace (< 5%)	moderate (30-45%)	trace (< 5%)
abundant (45-70%)	moderate (30-45%)	moderate (30-45%)	not detected
low (5-30%)	moderate (30-45%)	moderate (30-45%)	trace (< 5%)

Quartz	Chlorite
low (5-30%)	not detected
low (5-30%)	not detected
low (5-30%)	not detected
low (5-30%)	trace (< 5%)
trace (< 5%)	not detected
trace (< 5%)	not detected
low (5-30%)	trace (< 5%)
trace (< 5%)	not detected
trace (< 5%)	not detected
low (5-30%)	not detected
low (5-30%)	not detected
low (5-30%)	not detected

Table 2. Summary of post IR-IRSL burial age dating

Profile	Lab/field code	Equivalent dose (D_e) ± uncertainty (Gy)	Total dose rate ± error (Gy/ka)
Profile A			
	J0949/CC15-04	96.8 ± 3.55	3.002 ± 0.10
*Profile B**			
	J0948/CC15-03	110.0 ± 4.30	3.249 ± 0.13
Profile C			
	J0946/CC15-01	123.6 ± 5.35	3.009 ± 0.11
	J0947/CC15-02	116.6 ± 4.48	2.994 ± 0.11

*The dated sediment collected for Profile B was located 10 m below the soil profile

Age ± error (ka)
32.23 ± 1.6
33.86 ± 1.9
41.07 ± 2.3
38.95 ± 2.1

Table 3. Summary of chemical weathering indicies (see Supplementary Material for full geochem

Horizon	Zr (ppm)	Ti (wt. %)	Elemental losse* (τ)				
			Si	Al	Fe	Ca	Mg
Profile A							
A	285	1.21	-0.25	-0.16	-0.13	-0.24	-0.19
AC	278	1.17	-0.22	-0.17	-0.15	-0.12	-0.16
C	220	0.97	0.02	0.02	-0.1	0.1	-0.09
Parent debris	222	1.06					
Profile B							
A	369	1.18	-0.57	-0.52	-0.38	-0.65	-0.54
C1	272	1.13	-0.41	-0.33	-0.19	-0.6	-0.41
2C2	224	1.01	-0.29	-0.18	-0.06	-0.41	-0.24
Parent debris	165	0.85					
Profile C							
A	228	1.14	-0.4	-0.21	0.05	-0.56	-0.4
AC	162	0.91	-0.12	0.01	0.09	-0.09	0.08
C	166	1.26	-0.24	-0.06	0.47	0.52	0.8
Parent debris	148	0.83					
Profile D							
A	225	0.82	-0.15	-0.09	-0.03	-0.28	-0.2
C1	203	0.86	-0.08	0.02	0.13	-0.07	-0.03
Parent debris	193	0.77					

*footnotes: Elemental losses normalized to Zr content; negative tau values correspond to mass los

ıical dataset)

Na	K	CDF
-0.43	-0.06	
-0.33	-0.16	0.22
0.07	0.04	
-0.71	-0.45	
-0.6	-0.29	0.55
-0.4	-0.27	
-0.61	-0.29	
-0.19	-0.25	0.35
-0.31	-0.48	
-0.21	-0.1	
-0.1	-0.07	0.14

st of that element relative to parent material

Supplementary material

This document contains supporting material for *Storage and weathering of landslide debris in the eastern San Gabriel Mountains, California, USA*: *implications for mountain solute flux,* by Del Vecchio et al. This material includes detailed soil profile descriptions, an explanation of the post-IR IRSL luminescence burial dating protocol, an explanation of the integral transformation of San Antonio Canyon, and an explanation of the solute flux modeling used to calculate Figure 1 and Figure 7. This material also includes eight supplementary figures and four supplementary tables.

1. Soil profile descriptions

Profile A

Northing: 3788509 Easting: 435570 Elevation: 1187 m

A: 0 to 30 centimeters; dark brown (7.5YR 3/4) sandy clay loam, brown (7.5YR 4/4) moist; angular blocky structure; slightly hard, friable, moderately sticky, slightly plastic; common very fine tubular pores and common fine tubular pores; less than 5% subangular fine to medium gravel-sized rock fragments; clear smooth boundary.

AC: 30-62 centimeters; bright brown (7.5YR 5/6) clay loam, dull reddish brown (5YR 4/4) moist; angular blocky structure, medium hard, friable, moderately sticky, slightly plastic; common very fine tubular pores and common very coarse tubular roots; common fine tubular pores and common very fine tubular pores; about 25% angular medium to coarse gravel-sized rock fragments; gradual smooth boundary.

C: 62+ centimeters; brown (7.5YR 4/6) sandy clay loam, dull reddish brown (5YR 4/4) moist; angular blocky structure, medium hard, firm, slightly sticky, nonplastic; common fine to very fine tubular roots and common medium tubular roots; common very fine tubular pores; about 30% angular medium to coarse gravel-sized rock fragments. Lower boundary not observed.

Profile B

Northing: 3788450 Easting: 435315 Elevation: 1135 m

A: 0 to 20 centimeters; brown (10YR 4/4) loam, dark brown (10YR 3/4) moist; subangular blocky structure; slightly hard, friable, slightly sticky, nonplastic; common very tine tubular roots, common medium to very coarse tubular roots; common medium dendritic tubular pores and common fine tubular pores; about 10% gravel to very fine cobble-sized rock fragments; gradual wavy.

C1: 20-45 centimeters; dull brown (7.5YR 5/4) silt loam, dark brown (7.5YR 3/4) moist; subangular blocky structure, medium hard, friable, slightly to moderately sticky, nonplastic to slightly plastic; common very fine tubular roots, common medium tubular roots, common very fine tubular roots; common medium tubular pores, common very fine to fine tubular pores; less than 10% subrounded gravel-sized rock fragments; abrupt wavy boundary.

2C2: 45-90+ centimeters; brown (7.5YR 4/6) sandy loam, dark brown (7.5YR 3/4) moist; subangular blocky structure; slightly to medium hard, friable, slightly sticky, nonplastic; common very fine tubular roots and common very coarse tubular roots; common very fine to fine tubular pores; about 50% subrounded gravel-sized rock fragments. Lower boundary not observed.

Profile C
Northing: 3788276 Easting: 435081 Elevation: 1076 m

A: 0 to 45 centimeters; brown (7.5YR 5/4) clay loam, dull reddish brown (5YR 4/4) moist; angular blocky structure; slightly hard, firm, nonsticky, slightly plastic; common very fine and fine roots; common fine dendritic tubular pores, common medium-coarse tubular pores; about 5% subangular gravel-sized rock fragments; gradual smooth boundary.

AC: 45-70 centimeters; orange (7.5YR 6/6) sand, brown (7.5YR 4/4) moist; angular blocky structure, slightly hard, very friable, slightly sticky, nonplastic; common medium tubular roots and common very fine tubular roots; common medium tubular pores and common very fine tubular pores; about 40% angular fine to coarse gravel-sized rock fragments; gradual smooth boundary.

C: 70+ centimeters; dull yellow orange (10YR 6/4) sand, brown (10YR 4/6) moist; angular blocky structure, slightly hard, very friable, slightly sticky, nonplastic; common medium tubular roots; common medium tubular pores and common very fine tubular pores; about 50% angular gravel to cobble-sized rock fragments. Lower boundary not observed.

Profile D
Northing: 3788079 Easting: 434851 Elevation: 1040 m
A: 0 to 25 centimeters; dull yellowish brown (10YR 5/4) sandy loam, brown (10YR 4/6) moist; subangular blocky structure; slightly hard, friable, slightly sticky, nonplastic; common fine to medium tubular pores and common coarse to very coarse tubular pores; about 33% gravel to fine cobble-sized rock fragments; clear smooth boundary.

C1: 25-100 centimeters; yellowish brown (10YR 5/6) loamy sand, brown (10YR 4/6) moist; subangular blocky structure, slightly hard, loose, nonsticky, nonplastic; common fine to medium tubular roots and common very coarse tubular roots; common fine tubular pores; about 75% subrounded gravel to cobble-sized rock fragments; gradual smooth boundary.

2. Post-IR IRSL protocol

The methods used to obtain K-feldspar post-IR IRSL ages reported in the text use the protocol described by Rhodes (2015) and tested using age-controlled samples. The post-IR IRSL method has been tested near this location in the San Gabriel mountains (Scherler et al., 2016) and we use the same technique for this location. Each grain's equivalent dose was determined using a single aliquot regenerative-dose (SAR) protocol (Table

S1), modified for post-IR IRSL single-grain measurements (Murray and Wintle, 2000; Rhodes, 2015). The post-IR-IRSL measurements at 225 °C preceded by a 50 °C IR exposure. The elevated temperature, 225 °C IRSL measurement ("post-IR"), is used to estimate the equivalent dose.

Partial bleaching describes the bias introduced in the single-grain dose population of a sediment due to incomplete zeroing of the signal of a portion of the grains. Our statistical model posits that a well-zeroed sub-population should have a shared equivalent dose (D_e) value at the minimum dose value observed in the dose distribution. Variations in beta dose rate to individual grains, and differences in response to the protocol used, introduce a degree of over-dispersion between single grain D_e values; based on experience of single grains of quartz, an over-dispersion value of 15% has been used (Rhodes, 2015). Figure S1a-d shows the age population of each sample with the sub-population that meets this condition.

For these samples, we observe a sensitivity dependence on the minimum D_e value, similar to that described in Rhodes (2015). In order to avoid possible age underestimation introduced by this effect, the brightest 25% of single grain results were used in age calculations. The results demonstrated that these samples were moderately well bleached, with between 50 and 80% of grains sharing the common minimum D_e value.

Ages are calculated by dividing the equivalent dose by the environmental dose rate. The in-situ gamma dose rate was determined using an EG&G ORTEC MicroNOMAD NaI portable gamma spectrometer, while sediment beta dose rate contributions were estimated using ICP-OES (K) and ICP-MS (U, Th). An internal K concenbtration of 12.5 +/- 2.5% (Huntley and Baril, 1997), and a water content of 5 +/- 2.5% were assumed. Details of the total environmental dose rate calculation, including beta-dose and contribution from cosmic ray dose, can be found in Brown et al. (2015) and references therein.

3. Solute flux modeling

In Figure 1 we calculated the steady-state solute flux (W_{ss}) predicted in landscapes like the San Gabriel Mountains as a function of the total erosion rate (E)

This calculation follows the approach of Gabet and Mudd (2009),

$$W_{ss} = E\chi_m\left(1 - e^{-KT^{\sigma+1}/\sigma+1}\right)$$

where χ_m is the mass fraction of chemically mobile material, K and σ are empirically derived mineral weathering constants. T is the mineral residence time determined by,

$$T = \frac{\rho_{soil} h}{E}$$

where ρ_{soil} is soil density, and h is the soil thickness determined by

$$h = \frac{\ln(E/k_h)}{-\varphi}$$

where k_h is the maximum rate of soil production and φ is the soil production exponent (Heimsath et al., 1997), empirically determined for the San Gabriel Mountains by Heimsath et al. (2012). We further relate the erosion rate E to the average hillslope angle (S) using the nonlinear model of DiBiase et al. (2010),

$$S = S_c \frac{1}{E^*}\left(\sqrt{1+E^{*2}} - \ln\left(\frac{1}{2}\left(1+\sqrt{1+E^{*2}}\right)\right) - 1\right)$$

where E^* is a dimensionless erosion rate following Roering (2007),

$$E^* = \frac{2E(\rho_{rock}/\rho_{soil})L_H}{K_d S_c}$$

and ρ_{rock} is rock density, L_H is a characteristic hillslope length, K_d and S_c are empirically determined parameters for the San Gabriel Mountains.

In Figure 7 we calculated the time-dependent solute flux for each of five different mineral species (quartz, plagioclase feldspar, potassium feldspar, hornblende and biotite mica) following the approach of Yoo and Mudd (2008). In each timestep (dt) new soil mass m_0 is introduced to the soil column as,

$$m_0 = P\chi_i\rho_i(1-\theta)dt$$

where P is the soil production rate, χ_i is the concentration of mineral i in the parent material, ρ_i is the density of mineral i and θ is the relative soil porosity (volumetric fraction). The solute flux (W) is then calculated for each mineral i as

$$W_i = \frac{6a_i b_i \omega_i}{D\rho_i} T^{\alpha+\beta} m$$

where D is the mineral grain diameter, ρ_i, is mineral density, a_i, b_i, ω_i, α_i, and β_i, are mineral specific weathering parameters, T is the soil age and m is the accumulated soil mass per unit area. We assume a parent material of granodioritic composition, for both bedrock and debris soils, since the weathered surface of landslide debris is <5% of the total landslide debris volume. Please see Yoo and Mudd (2008) for the full derivation of this model and additional commentary about its implementation.

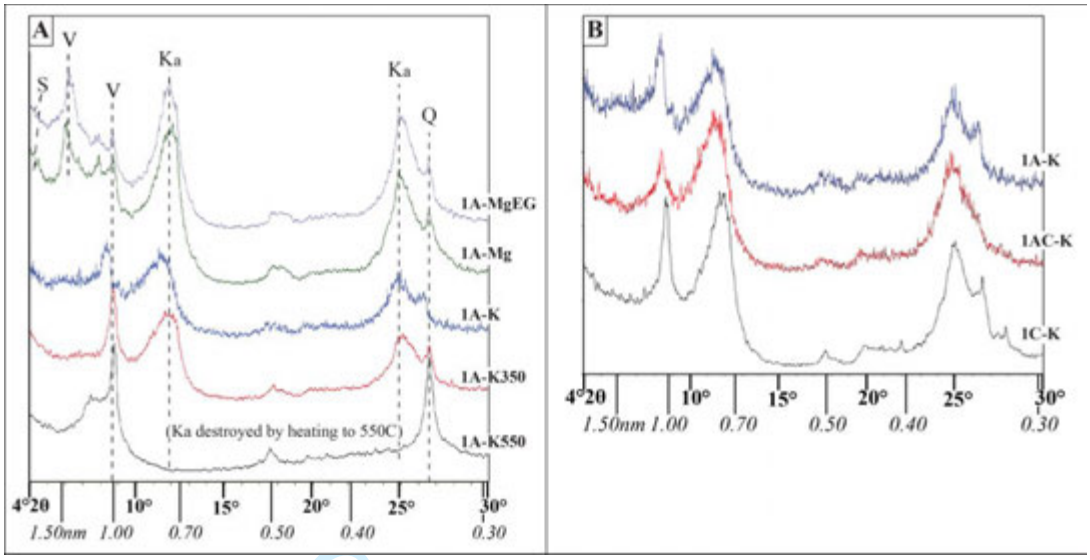

Supplemental Figure 1. Example XRD spectra and mineralogical interpretations of the clay-sized particle fraction for: **(A)** Sample 1A and **(B)** Profile 1 (all three horizons, K-treated samples only). Y-axis units are relative peak counts for each spectrum. X-axis indicates scan angle (°2θ) and d-spacing (nm). Treatments are K-saturation (K), K-saturation heated to 350°C (K350) and 550°C (K550), Mg-saturation (Mg), and Mg-saturation with ethylene glycol solvation (MgEG). Diagnostic peaks are indicated as Ka = kaolinite, Q = quartz, S = smectite, V = vermiculite. Mineralogical composition was generally similar in all three horizons (A, AC, and C) of Profile 1. For more information on the clay-sized X-ray diffraction data for individual horizon samples, see the Supplement Data File.

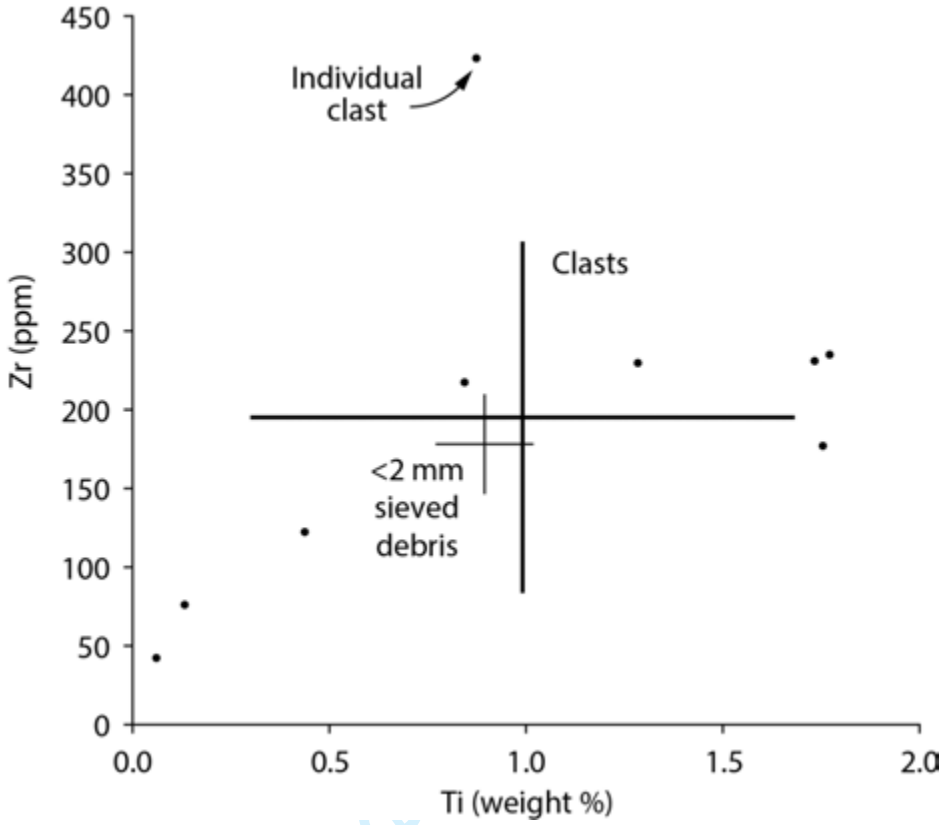

Supplemental Figure 2. Comparison of measurements from individual clasts to the bulk sample material sieved < 2 mm. Clasts were chosen to represent the local variety in source rock lithology and weathering. There is no significant difference between bulk sample material and an average of individual clast analyses, indicating that sieving samples < 2 mm effectively averages over the potential geochemical variability in source rock clasts in parent material.

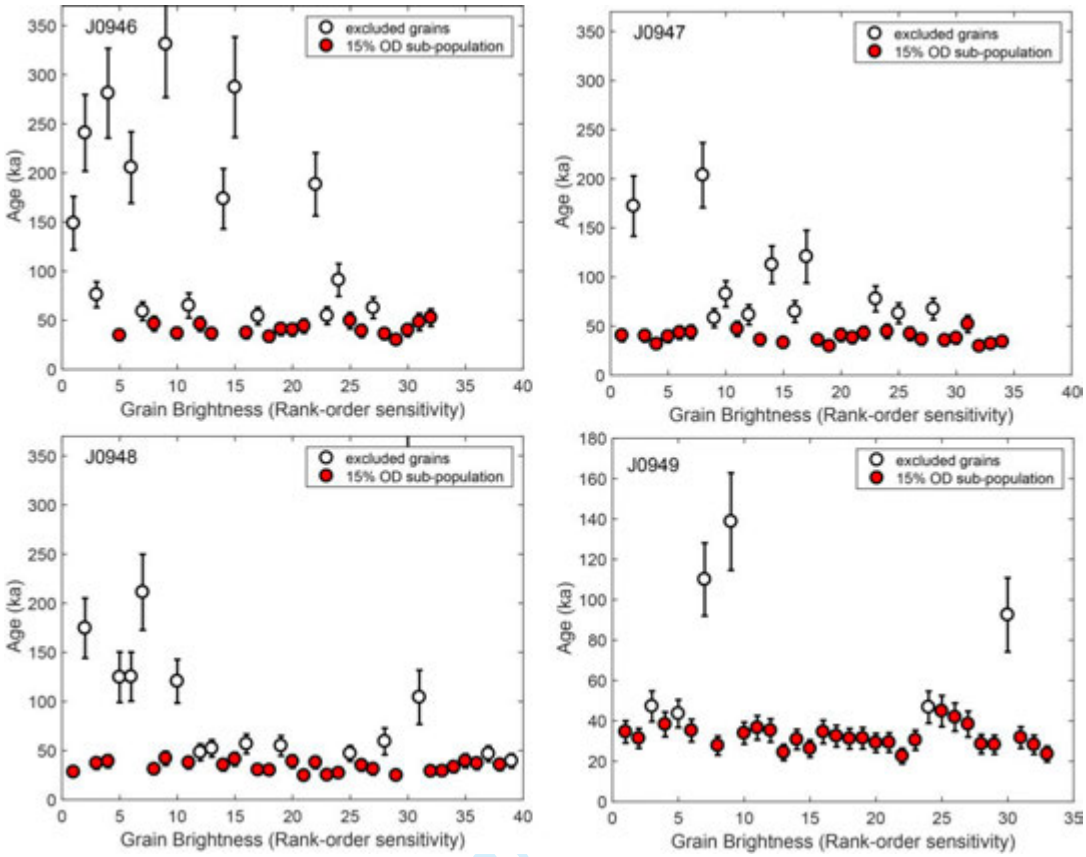

Supplemental Figure 3. Single-grain age distributions for post-IR IRSL signals in each sample. Symbols are plotted in rank order sensitivity from the brightest grain in decreasing sensitivity order. Grains represented by closed symbols are included in the equivalent dosing estimation, while open symbols are excluded grains employing a standard overdispersion (OD) value of 15% (see Rhodes, 2015 for details).

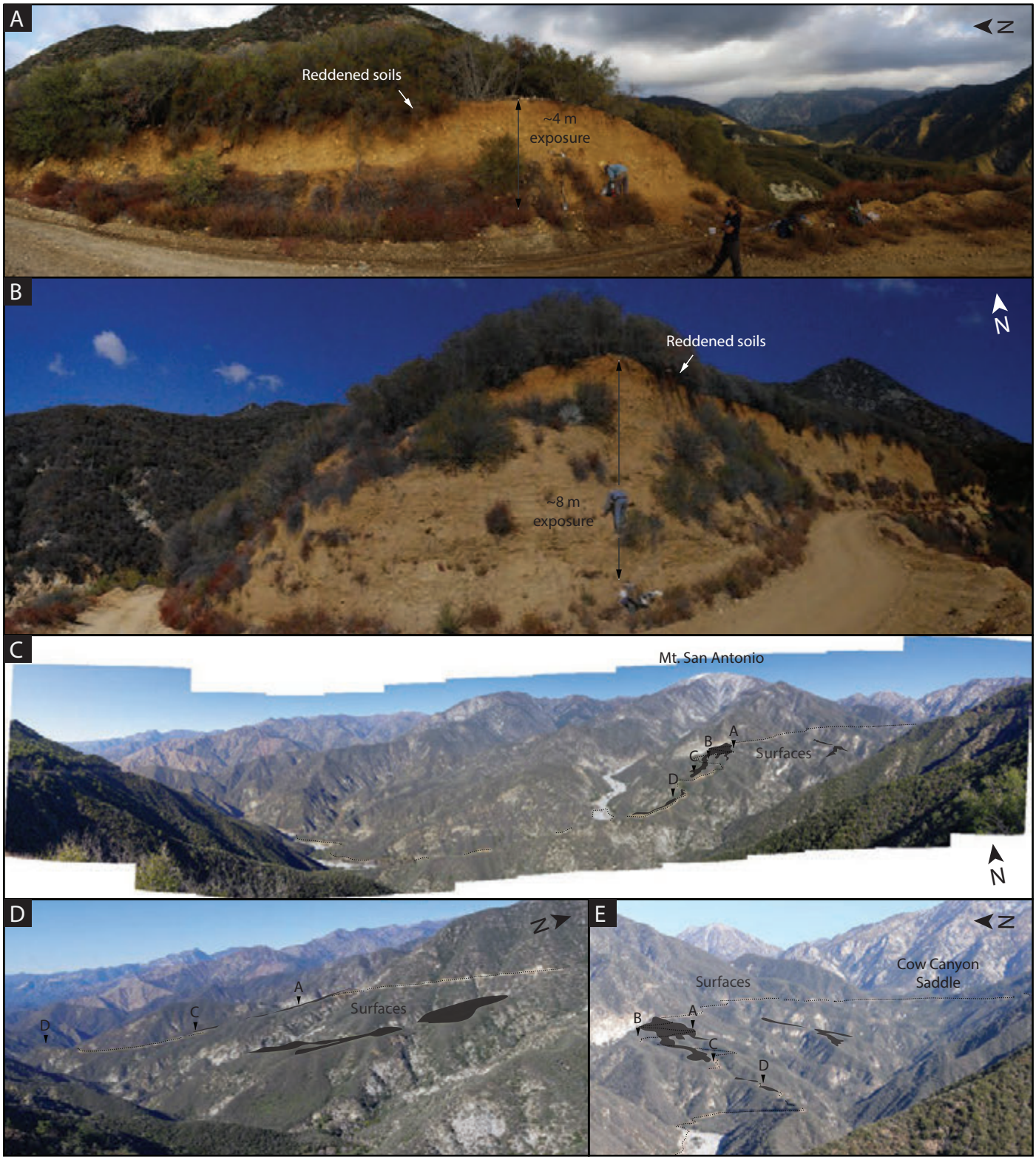

Supplemental Figure 4. Panoramic color photographs of Cow Canyon and deposits. A. Location of site A at deposit roadcut. B. Location of site C at deposit roadcut. Bedrock is exposed several meters below the elevation of the road, outside of the photograph. Note distinctly reddened soil at top of exposures in A and B. North-looking perspective of the East Fork of the San Gabriel River below Mt. San Antonio. D. West-looking perspective of Cow Canyon deposits similar to figure 4A. E. East-looking perspective of Cow Canyon deposits.

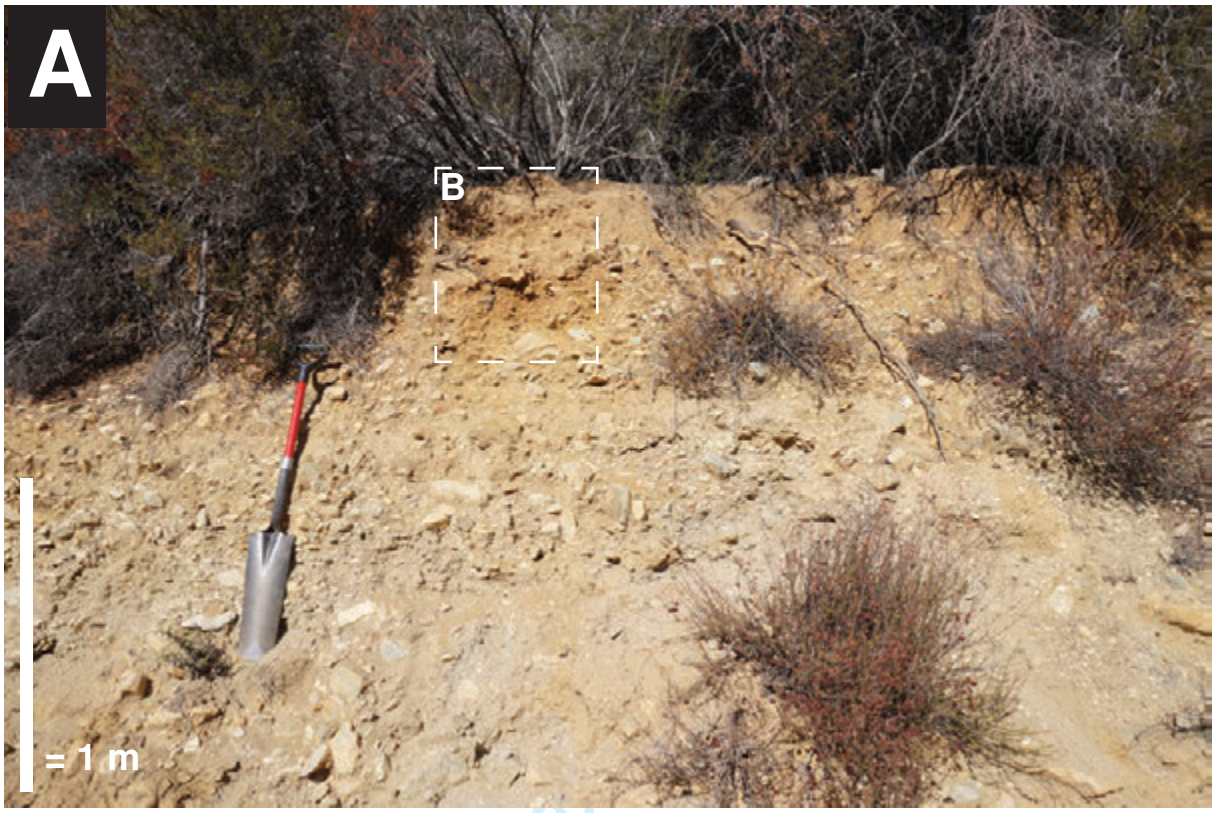

Supplemental Figure 4: Field photographs of the parent material and soil development, visible as a roadcut, described in Profile A (elevation 1187 m). (A) View of soil profile and underlying parent material. (B) Close-up view of the same soil profile

Supplemental Figure 6: Field photographs of the parent material and soil development, visible as a roadcut, described in Profile B (elevation 1135 m). (A) Close-up view of upper 20 cm of soil profile. (B) View of the same soil profile with rocky parent material below.

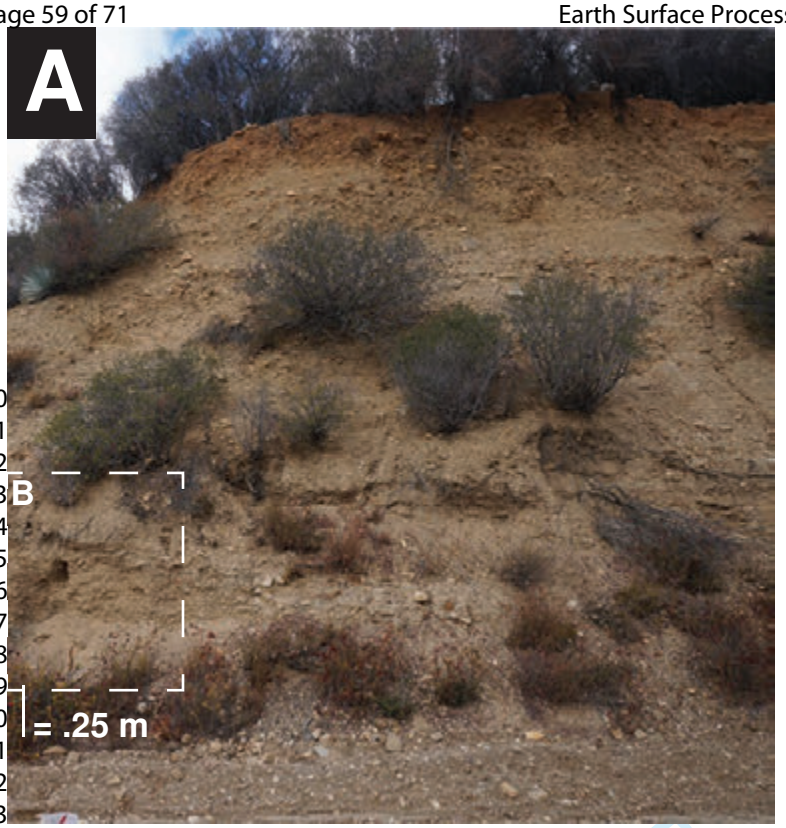

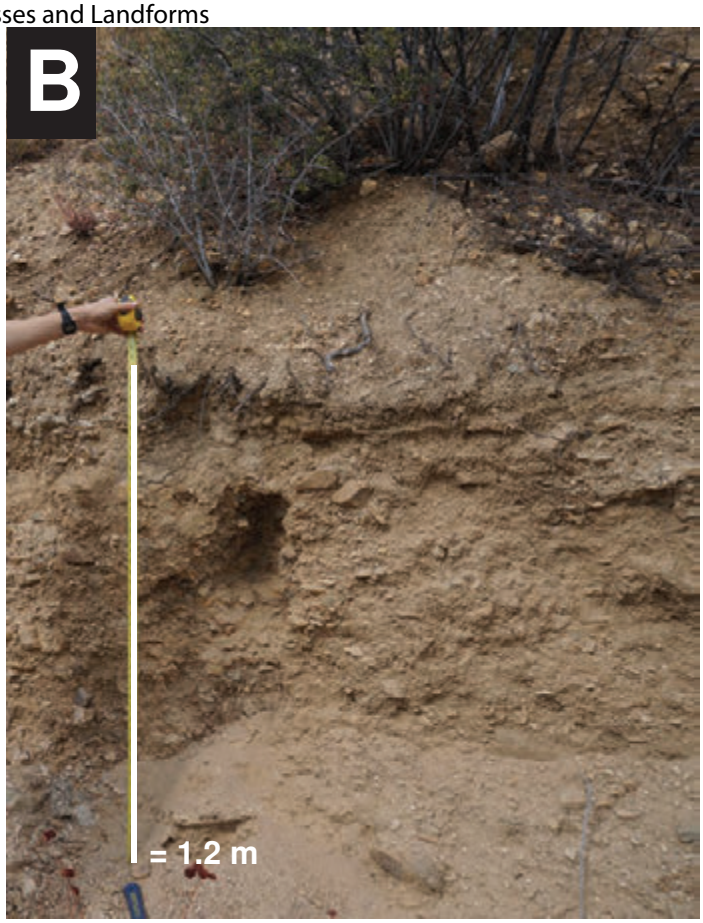

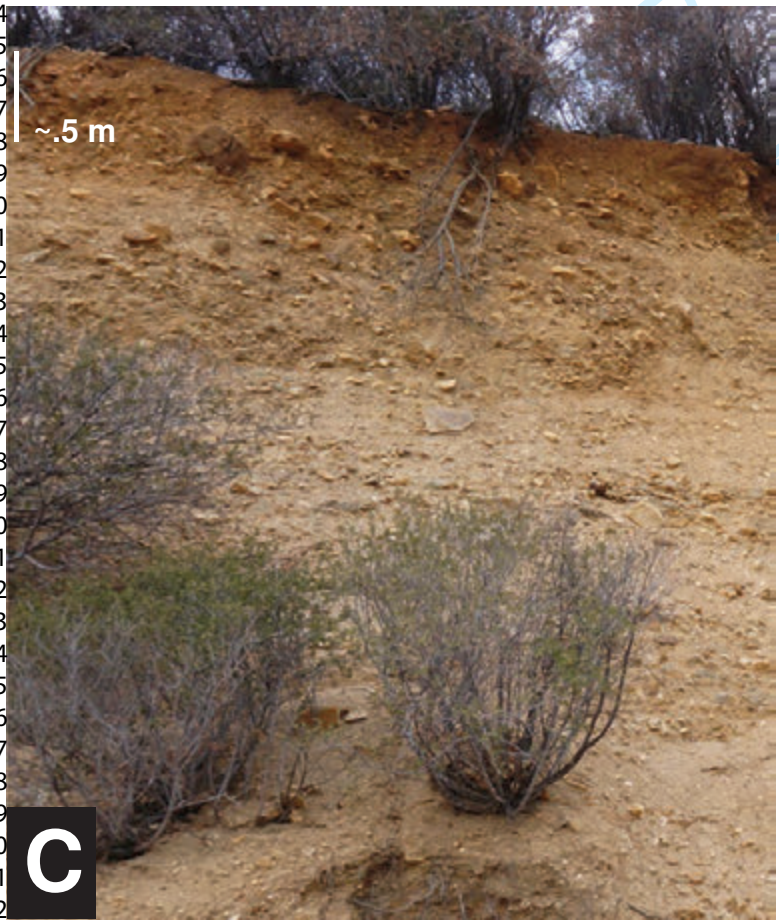

Supplemental Figure 7: Field photographs of the parent material and soil development, visible as a roadcut, described in Profile C (elevation 1076 m). (A) The entirety of the debris package, including unaltered parent material below a reddened soil profile. (B) Close-up view of unaltered parent material and location of IRSL samples CC15-01 and CC15-02. (C) Close-up view of location of soil profile description.

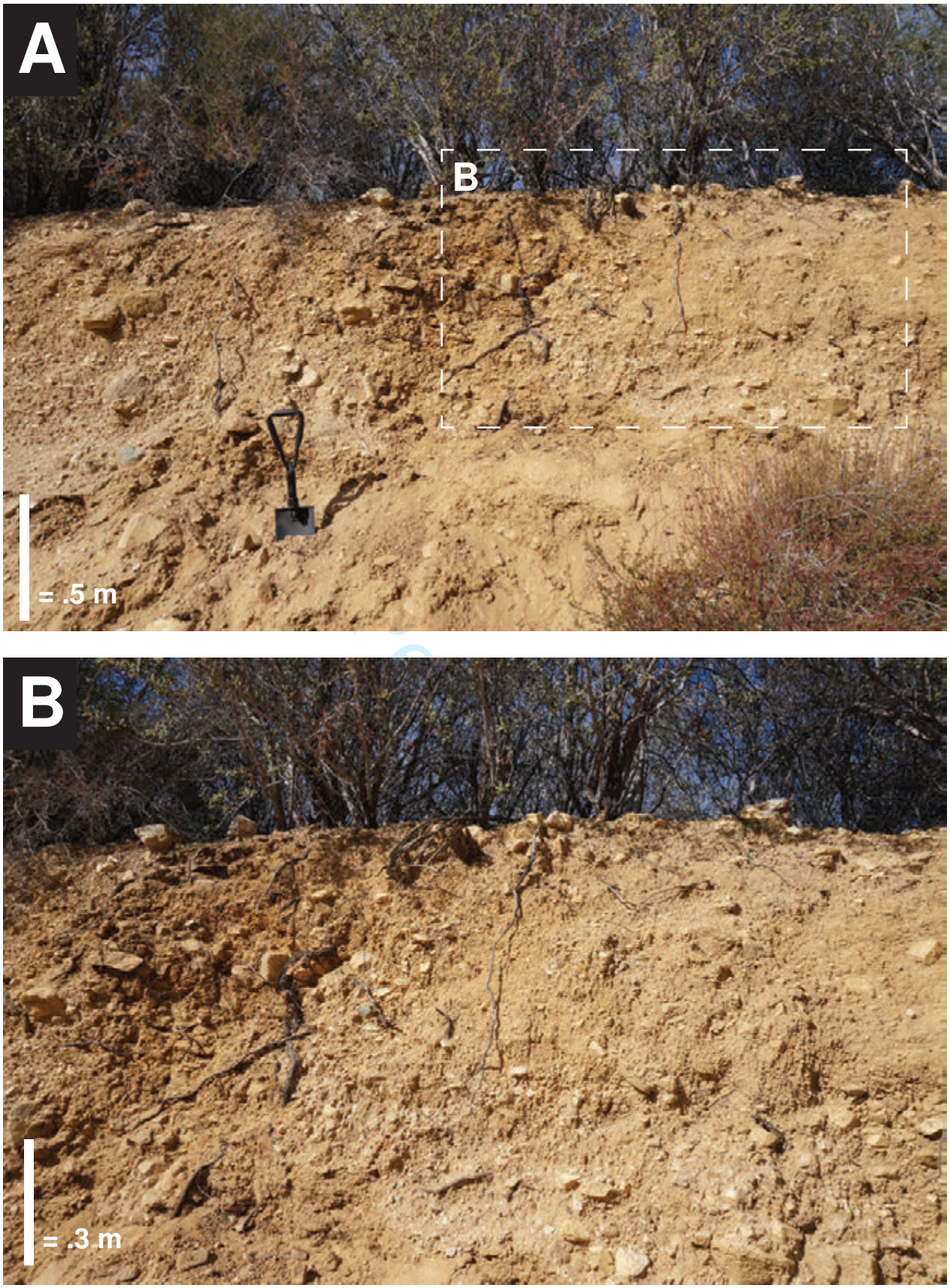

Supplemental Figure 8: Field photographs of the parent material and soil development, visible as a roadcut, described in Profile D (elevation 1040 m). (A) View of soil profile and underlying parent material. (B) Close-up view of the same soil profile.

Supplemental references

DiBiase, R. A., Whipple, K. X., Heimsath, A. M., & Ouimet, W. B. (2010). Landscape form and millennial erosion rates in the San Gabriel Mountains, CA. *Earth and Planetary Science Letters*, *289*(1), 134-144.

Gabet, E. J., & Mudd, S. M. (2009). A theoretical model coupling chemical weathering rates with denudation rates. *Geology*, *37*(2), 151-154.

Heimsath, A. M., Dietrich, W. E., Nishiizumi, K., & Finkel, R. C. (1997). The soil production function and landscape equilibrium. *Nature*, *388*(6640), 358-361.

Heimsath, A. M., DiBiase, R. A., & Whipple, K. X. (2012). Soil production limits and the transition to bedrock-dominated landscapes. *Nature Geoscience*, *5*(3), 210-214.

Rhodes, E.J., 2015, Dating sediments using potassium feldspar single-grain IRSL: initial methodological considerations: Quaternary International, v. 362, p. 14–22.

Roering, J. J., Kirchner, J. W., & Dietrich, W. E. (1999). Evidence for nonlinear, diffusive sediment transport on hillslopes and implications for landscape morphology. *Water Resources Research*, *35*(3), 853-870.

Roering, J. J., Perron, J. T., & Kirchner, J. W. (2007). Functional relationships between denudation and hillslope form and relief. *Earth and Planetary Science Letters*, *264*(1), 245-258.

Yoo, K., & Mudd, S. M. (2008). Toward process-based modeling of geochemical soil formation across diverse landforms: A new mathematical framework. *Geoderma*, *146*(1), 248-260.

Table S1. Model parameters used in the calculation of Figure 1 and Figure 7

Parameter	Value	Units	Source
χ_m	0.8	unitless	Hyndman (1972)
K	0.0032	yr^{-1}	Yoo and Mudd (2009)
σ	-0.27	unitless	White and Brantley (2003)
ρ_{soil}	1650	kg m^{-3}	assumed
ρ_{rock}	2750	kg m^{-3}	assumed
φ	-0.03	cm^{-1}	Heimsath et al (2012)
k_h	962	t $km^{-2}yr^{-1}$	>30° slopes in Heimsath et al (2012)
L_h	75	m	DiBiase et al (2010)
K_d	0.008	m^2yr^{-1}	DiBiase et al (2010)
S_c	39	degrees	DiBiase et al (2010)

Mineral specific parameters

Parameter	Value				Units	Source
	K-feldspar	Plagioclase feldspar	Hornblende	Biotite		
ρ_i	2600	2600	3200	3000	kg m-3	Gabet an
a_i	1.020x10-5	1.093x10-5	0.674x10-5	.509x10-ol	m-2 yr	White an
bi	13.6	13.6	13.6	13.6	unitless	White an
αi	-0.647	-0.564	-0.623	-0.603	unitless	White an
βi	0.2	0.2	0.2	0.2	unitless	White an
ωi	0.2782	0.263	0.8212	0.4335	kg mol-1	Gabet an

ıd Mudd (2009)
d Brantley (2003)
d Brantley (2003)
d Brantley (2003)
d Brantley (2003)
ıd Mudd (2009)

Table S2. SAR protocol for post-IR IRSL measurements.

Step	Measurement
1	Natural, Regenerative Dose
2	Preheat 250°C, 60s
3	IR diodes at 50 oC
4	IR diodes at 225 °C
5	Test Dose
6	Preheat 250°C, 60s
7	IR diodes at 50 oC
8	IR diodes at 225 °C
9	Hot bleach IR diodes at 290 °C, 40s
Repeat from step 1	

Table S3. Measurements, post IR-IRSL burial age dating

Lab Code	J0946	J0947	J0948
Field Code	CC15-01	CC15-02	CC15-03
De (Gy)	123.6	116.62	110.01
uncertainty	5.354744065	4.484304825	4.296158754
measured	4.75	3.83	3.69
Total dose rate, Gy/ka	3.009484513	2.993786339	3.248656284
error	0.112343211	0.112570638	0.125973098
% error	3.732972	3.760143	3.877699
AGE (ka)	41.07015652	38.95401568	33.86323156
error	2.348697778	2.095003711	1.863631055
% error	5.718745623	5.378145679	5.503405815

J0949 CC15-04
96.78
3.545059571
2.97
3.002459741
0.101392813
3.376992
32.23357126
1.605921135
4.982138411

Table S4. Full analytical data from XRF and XRD analyses

Soil samples

Pofile	rofile field cod	Horizon	LOI (%)	SiO2	TiO2	Al2O3	Fe2O3	MnO
C	CC-01	A	12.59	58.09	1.14	21.77	9.25	0.13
	analytic uncertainty		*0.02*	*0.03*	*0.01*	*0.02*	*0.00*	*0.00*
	CC-01	AC	7.95	60.22	0.91	19.93	6.85	0.10
	a. u.		*0.04*	*0.01*	*0.00*	*0.01*	*0.00*	*0.00*
	CC-01	C	6.84	54.02	1.26	19.11	9.46	0.14
	a. u.		*0.07*	*0.01*	*0.00*	*0.02*	*0.01*	*0.00*
	CC-01	PM	5.33	62.96	0.83	18.03	5.74	0.10
	a. u.		*0.08*	*0.01*	*0.00*	*0.03*	*0.01*	*0.00*
A	CC-02	A	16.74	59.34	1.21	20.54	8.48	0.15
	a. u.		*0.15*	*0.01*	*0.00*	*0.03*	*0.01*	*0.01*
	CC-02	AC	9.94	60.05	1.17	19.89	8.12	0.13
	a. u.		*0.03*	*0.01*	*0.00*	*0.01*	*0.00*	*0.00*
	CC-02	C	9.14	62.01	0.97	19.36	6.77	0.11
	a. u.		*0.05*	*0.01*	*0.00*	*0.02*	*0.00*	*0.00*
	CC-02	PM	8.85	61.50	1.06	19.09	7.61	0.09
	a. u.		*0.07*	*0.01*	*0.00*	*0.02*	*0.01*	*0.00*
D	CC-03	A	7.03	64.79	0.82	17.56	6.09	0.08
	a. u.		*0.04*	*0.02*	*0.00*	*0.00*	*0.01*	*0.00*
	CC-03	C1	6.54	63.56	0.86	17.75	6.43	0.10
	a. u.		*0.06*	*0.00*	*0.00*	*0.02*	*0.01*	*0.00*
	CC-03	PM	5.25	65.56	0.77	16.62	5.40	0.09
	a. u.		*0.07*	*0.01*	*0.00*	*0.01*	*0.00*	*0.00*
B	CC-04	A	11.30	59.92	1.18	19.11	7.94	0.15
	a. u.		*0.03*	*0.02*	*0.00*	*0.00*	*0.01*	*0.00*
	CC-04	C1	8.80	60.52	1.13	19.79	7.63	0.12
	a. u.		*0.10*	*0.02*	*0.00*	*0.03*	*0.01*	*0.00*
	CC-04	2C2	7.09	59.94	1.01	19.81	7.33	0.10
	a. u.		*0.01*	*0.01*	*0.00*	*0.01*	*0.01*	*0.00*
	CC-04	PM	5.30	62.40	0.85	17.79	5.74	0.10
	a. u.		*0.05*	*0.01*	*0.00*	*0.01*	*0.00*	*0.00*

Rock fragments

Field code	Lithology	SiO2	TiO2	Al2O3	Fe2O3	MnO
CC-FGB	fine-grained basalt	61.30	1.78	15.86	8.42	0.11
CC-QFL	quartz/felsic	69.52	0.03	19.14	0.23	0.00
CC-GN	gneiss	47.82	1.76	16.29	12.27	0.17
CC-PAN	porphyritic andesite	56.52	1.28	16.45	7.50	0.11
CC-FAN	fine-grained andesite	65.84	0.86	15.58	5.55	0.10
CC-MPG	micaceous pegmatitic	72.43	0.10	15.94	0.94	0.02
CC-RF-1(	grussified granodiorite/schist, C hc	65.70	0.41	18.94	2.94	0.05
CC-RF-1(	grussified granodiorite/schist, AC h	58.01	0.83	21.01	5.46	0.10
CC-RF-1(	grussified granodiorite/schist, A hc	59.78	1.74	17.64	8.95	0.11

MgO	CaO	Na2O	K2O	P2O5	Rb	Sr	Ba	Zr	Y
2.52	2.37	2.16	2.20	0.13	65.59	331.37	888.50	227.65	28.98
0.00	*0.00*	*0.01*	*0.00*	*0.00*	*0.58*	*1.15*	*4.93*	*1.00*	*0.58*
3.23	3.48	3.23	1.66	0.14	39.83	463.15	705.05	161.87	21.73
0.01	*0.00*	*0.00*	*0.00*	*0.00*	*0.58*	*0.58*	*7.94*	*1.00*	*0.00*
5.54	6.02	2.81	1.17	0.24	27.19	541.72	562.11	166.38	25.76
0.01	*0.01*	*0.01*	*0.00*	*0.00*	*0.58*	*0.58*	*1.15*	*0.00*	*0.00*
2.74	3.52	3.65	2.02	0.18	47.89	544.00	772.86	148.23	17.25
0.00	*0.00*	*0.01*	*0.00*	*0.00*	*0.58*	*0.00*	*4.62*	*1.15*	*0.58*
2.90	2.46	2.19	2.35	0.11	86.88	330.71	941.67	285.07	31.63
0.01	*0.01*	*0.01*	*0.00*	*0.00*	*0.58*	*0.58*	*6.56*	*0.58*	*0.58*
2.92	2.76	2.53	2.06	0.10	69.21	384.56	899.77	278.33	29.24
0.01	*0.00*	*0.01*	*0.01*	*0.01*	*0.58*	*0.58*	*4.73*	*0.58*	*0.58*
2.51	2.73	3.18	2.01	0.10	59.06	446.10	896.59	220.11	23.11
0.00	*0.01*	*0.01*	*0.00*	*0.00*	*0.58*	*1.15*	*4.04*	*1.00*	*0.00*
2.79	2.52	3.00	1.95	0.16	64.73	411.78	778.58	221.98	27.06
0.00	*0.01*	*0.01*	*0.00*	*0.01*	*0.00*	*0.58*	*0.58*	*0.58*	*0.58*
1.85	2.66	3.28	2.51	0.10	67.41	433.11	1034.02	224.80	27.97
0.01	*0.00*	*0.00*	*0.00*	*0.00*	*0.58*	*0.58*	*4.04*	*1.00*	*0.00*
2.04	3.10	3.38	2.34	0.19	62.06	461.15	975.80	202.94	29.60
0.01	*0.01*	*0.01*	*0.00*	*0.01*	*0.00*	*1.73*	*2.65*	*0.58*	*0.58*
2.01	3.18	3.58	2.40	0.16	57.70	465.45	1017.10	193.50	24.28
0.00	*0.00*	*0.01*	*0.00*	*0.00*	*0.58*	*0.00*	*4.62*	*0.58*	*1.00*
3.28	2.94	2.43	2.60	0.17	87.18	352.48	921.41	368.64	33.07
0.00	*0.00*	*0.01*	*0.01*	*0.00*	*0.58*	*0.58*	*3.21*	*1.00*	*0.58*
3.11	2.47	2.44	2.46	0.10	81.14	338.43	922.10	271.55	31.07
0.01	*0.00*	*0.01*	*0.00*	*0.00*	*0.00*	*0.58*	*8.54*	*0.58*	*0.58*
3.31	2.98	2.98	2.11	0.15	55.25	416.55	807.63	223.52	26.19
0.01	*0.00*	*0.00*	*0.01*	*0.00*	*0.58*	*0.00*	*5.51*	*0.58*	*0.58*
3.19	3.71	3.69	2.11	0.20	46.81	483.98	688.14	164.73	17.60
0.00	*0.00*	*0.00*	*0.00*	*0.00*	*0.52*	*0.40*	*2.16*	*0.09*	*0.50*

MgO	CaO	Na2O	K2O	P2O5	Rb	Sr	Ba	Zr	Y
2.35	3.26	5.21	1.12	0.43	26.00	316.32	314.15	240.49	35.75
0.10	3.48	7.05	0.31	0.01	2.08	746.01	194.29	43.64	4.16
8.50	7.86	2.94	1.63	0.50	34.92	624.40	706.95	182.03	29.63
4.24	6.04	5.05	2.37	0.27	57.50	338.60	326.89	235.32	27.68
0.87	2.08	6.21	2.49	0.25	66.67	159.80	519.62	432.84	47.62
0.24	1.64	3.23	5.08	0.06	81.60	687.95	2009.12	77.47	6.20
1.09	3.83	4.82	1.85	0.11	33.04	767.19	1012.94	124.94	5.16
2.35	5.82	4.64	1.22	0.31	24.91	926.70	792.84	223.11	5.19
2.41	2.42	4.44	2.03	0.30	58.25	345.16	502.64	236.22	25.89

Nb	Cs	Sc	V	Cr	Co	Ni	Cu	Zn	Ga
23.26	6.48	19.83	160.54	101.81	35.46	75.88	74.74	85.04	27.07
0.58	*3.79*	*0.58*	*0.58*	*1.73*	*3.61*	*1.15*	*0.58*	*1.53*	*0.58*
15.21	2.53	18.11	135.07	82.93	27.88	76.41	79.67	78.22	22.45
0.00	*2.52*	*0.58*	*1.53*	*0.58*	*2.52*	*1.53*	*1.15*	*1.00*	*0.58*
16.82	-5.01	22.90	189.28	148.13	50.45	118.43	110.92	95.53	21.83
0.58	*2.52*	*1.15*	*1.53*	*2.00*	*2.00*	*1.15*	*1.53*	*1.00*	*0.58*
9.86	-1.41	14.44	113.38	63.38	46.12	55.98	48.24	75.70	19.72
0.58	*1.53*	*1.53*	*0.58*	*1.00*	*0.58*	*0.00*	*2.08*	*1.53*	*0.58*
29.23	0.80	18.82	159.75	101.70	38.04	65.26	62.86	106.50	25.62
0.58	*1.53*	*1.15*	*1.00*	*1.53*	*1.53*	*1.15*	*0.58*	*1.15*	*0.58*
23.69	1.48	18.14	150.64	94.01	36.64	61.07	63.29	114.37	25.91
0.58	*3.51*	*0.58*	*3.21*	*1.53*	*1.00*	*0.00*	*0.00*	*1.73*	*0.58*
18.34	0.74	16.14	125.47	75.57	32.28	50.99	132.43	87.68	23.85
0.58	*4.16*	*1.15*	*1.73*	*0.58*	*2.08*	*1.15*	*0.58*	*1.53*	*0.58*
18.29	0.00	15.36	138.97	73.51	14.99	44.62	53.39	87.04	23.41
0.58	*1.00*	*0.00*	*1.15*	*1.73*	*0.58*	*0.58*	*0.58*	*1.15*	*0.58*
16.13	4.30	15.42	106.48	66.69	33.70	37.29	38.72	78.52	19.36
1.00	*6.56*	*0.58*	*2.00*	*3.61*	*2.08*	*0.58*	*0.00*	*1.73*	*1.00*
18.90	0.35	16.76	118.77	60.99	32.10	37.09	46.01	87.74	19.97
0.58	*6.66*	*1.15*	*2.00*	*0.00*	*2.65*	*0.58*	*0.00*	*1.00*	*0.58*
17.94	0.00	14.42	101.32	59.46	42.57	38.35	34.48	79.51	17.94
0.00	*6.08*	*0.58*	*1.00*	*0.58*	*2.31*	*0.58*	*0.58*	*1.53*	*1.00*
29.69	3.76	18.41	149.56	101.08	34.57	78.54	55.62	130.40	23.67
0.58	*4.16*	*1.53*	*1.15*	*0.58*	*1.53*	*0.58*	*1.53*	*1.15*	*0.00*
26.68	2.55	18.27	147.29	98.31	47.88	69.44	62.50	110.01	24.85
0.58	*7.37*	*0.58*	*2.89*	*1.15*	*2.08*	*1.15*	*0.00*	*0.58*	*0.58*
19.02	3.59	16.86	135.98	92.21	33.73	71.04	67.81	531.36	25.12
0.58	*4.73*	*2.31*	*1.53*	*1.53*	*3.21*	*1.00*	*0.00*	*2.31*	*0.58*
11.62	4.93	14.78	118.62	77.09	28.16	62.65	58.78	75.33	19.71
0.87	*2.77*	*1.72*	*0.48*	*2.62*	*2.00*	*0.48*	*0.47*	*1.29*	*0.50*

Nb	Cs	Sc	V	Cr	Co	Ni	Cu	Zn	Ga
19.50	0.00	17.33	177.66	13.00	17.33	20.58	30.33	96.41	18.42
-7.27	1.04	0.00	9.35	3.12	-31.17	1.04	0.00	11.43	17.66
20.11	0.00	24.34	240.24	192.61	56.09	141.81	62.44	74.08	19.05
21.30	-4.26	20.23	149.07	93.70	34.07	53.24	40.46	106.48	18.10
29.63	2.12	10.58	23.28	12.70	-7.41	1.06	2.12	73.02	22.22
-4.13	2.07	0.00	19.63	5.16	-21.69	1.03	2.07	25.82	13.43
1.03	1.03	4.13	53.69	10.33	34.07	13.42	19.62	38.20	20.65
6.23	1.04	6.23	102.74	22.83	30.09	30.09	28.02	74.72	20.75
22.65	7.55	18.34	181.21	21.57	52.85	21.57	29.12	97.08	22.65

La	Ce	Pr	Nd	Sm	Hf	Ta	Pb	Th
32.79	65.59	6.86	26.31	4.58	5.34	-2.29	21.35	-1.91
4.16	*5.03*	*0.00*	*2.00*	*2.00*	*1.53*	*3.46*	*1.15*	*1.15*
21.36	49.61	6.52	23.18	5.79	5.07	-1.81	13.76	-2.17
5.77	*5.51*	*0.00*	*1.53*	*1.53*	*0.58*	*3.51*	*2.52*	*2.00*
26.12	60.83	7.51	31.13	7.16	4.29	-2.50	8.59	-5.37
3.06	*1.53*	*1.00*	*3.61*	*0.58*	*1.73*	*2.52*	*1.00*	*1.00*
24.29	51.05	4.93	18.31	2.46	3.52	1.76	9.15	-0.70
1.00	*2.52*	*0.58*	*2.31*	*1.53*	*1.53*	*1.53*	*1.15*	*2.52*
39.64	79.68	9.61	34.43	8.01	6.01	1.60	18.02	-4.40
5.57	*4.04*	*0.00*	*1.53*	*0.58*	*1.00*	*2.52*	*2.65*	*0.58*
35.53	70.69	8.14	32.20	6.66	5.92	-0.74	16.29	-2.22
6.08	*3.06*	*0.58*	*2.65*	*1.00*	*0.58*	*1.15*	*1.15*	*0.00*
25.68	57.23	5.50	22.38	4.40	4.77	0.00	16.14	-4.40
2.52	*3.61*	*1.00*	*3.79*	*1.00*	*1.15*	*2.00*	*1.15*	*1.00*
35.47	64.73	7.31	25.96	6.58	5.12	0.73	14.99	-1.46
8.50	*0.00*	*1.53*	*4.16*	*2.65*	*0.58*	*0.58*	*2.08*	*1.15*
36.57	72.78	9.68	34.78	6.10	5.74	0.72	15.06	#DIV/0!
4.36	*2.08*	*1.00*	*3.21*	*1.15*	*2.31*	*1.53*	*1.73*	*1.15*
48.51	87.38	10.34	39.23	7.13	4.28	-1.43	14.98	#DIV/0!
4.51	*2.31*	*0.58*	*0.58*	*1.53*	*1.00*	*1.53*	*0.00*	*1.15*
32.71	62.97	7.04	25.68	6.33	4.57	-5.98	12.31	#DIV/0!
8.54	*7.64*	*0.58*	*2.31*	*1.00*	*1.53*	*1.15*	*1.15*	*1.73*
40.21	83.05	9.39	33.82	7.14	7.89	-4.13	24.05	#DIV/0!
6.66	*5.51*	*1.53*	*4.36*	*0.58*	*0.00*	*2.52*	*1.53*	*2.08*
31.80	67.61	7.68	31.07	7.31	6.58	-4.02	17.91	#DIV/0!
1.00	*0.58*	*1.00*	*3.21*	*1.15*	*1.00*	*1.53*	*0.58*	*1.15*
27.27	55.25	6.46	25.12	4.31	5.02	-4.31	16.50	#DIV/0!
12.74	*12.10*	*0.00*	*3.06*	*1.00*	*1.15*	*2.65*	*1.15*	*2.52*
22.18	48.22	6.34	23.23	4.58	4.58	-3.17	13.38	-2.82
3.10	*4.89*	*0.86*	*2.28*	*1.31*	*1.80*	*2.28*	*0.50*	*0.50*

La	Ce	Pr	Nd	Sm	Hf	Ta	Pb	Th	U
24.92	45.50	5.42	26.00	5.42	4.33	2.17	3.25	-1.08	3.25
0.00	4.16	2.08	6.23	2.08	2.08	2.08	10.39	1.04	5.20
30.69	63.50	9.52	33.87	7.41	4.23	-7.41	1.06	-3.17	1.06
17.04	38.33	5.32	20.23	4.26	5.32	-4.26	2.13	-2.13	0.00
41.27	69.85	6.35	25.40	6.35	8.47	3.17	7.41	3.17	4.23
9.30	23.76	1.03	4.13	2.07	4.13	1.03	42.35	-2.07	1.03
10.33	29.94	5.16	15.49	1.03	3.10	4.13	9.29	-4.13	3.10
44.62	58.11	4.15	14.53	4.15	5.19	3.11	5.19	-8.30	2.08
23.73	43.15	6.47	29.12	4.31	2.16	-5.39	5.39	-3.24	3.24

As	Mo	S
2.17	2.17	150.58
-10.39	4.16	151.70
1.06	2.12	134.40
-3.19	3.19	113.93
6.35	2.12	153.45
-1.03	3.10	139.45
-10.33	2.07	265.37
-10.38	3.11	120.38
1.08	3.24	145.62